



Publication Year	2017
Acceptance in OA @INAF	2021-01-07T08:20:54Z
Title	Effects of waveform model systematics on the interpretation of GW150914
Authors	Abbott, B. P.; Abbott, R.; Abbott, T. D.; Abernathy, M. R.; Acernese, F.; et al.
DOI	10.1088/1361-6382/aa6854
Handle	http://hdl.handle.net/20.500.12386/29510
Journal	CLASSICAL AND QUANTUM GRAVITY
Number	34

Effects of waveform model systematics on the interpretation of GW150914

B. P. Abbott *et al.**

Parameter estimates of GW150914 were obtained using Bayesian inference, based on three semi-analytic waveform models for binary black hole coalescences. These waveform models differ from each other in their treatment of black hole spins, and all three models make some simplifying assumptions, notably to neglect sub-dominant waveform harmonic modes and orbital eccentricity. Furthermore, while the models are calibrated to agree with waveforms obtained by full numerical solutions of Einstein's equations, any such calibration is accurate only to some non-zero tolerance and is limited by the accuracy of the underlying phenomenology, availability, quality, and parameter-space coverage of numerical simulations. This paper complements the original analyses of GW150914 with an investigation of the effects of possible systematic errors in the waveform models on estimates of its source parameters. To test for systematic errors we repeat the original Bayesian analyses on mock signals from numerical simulations of a series of binary configurations with parameters similar to those found for GW150914. Overall, we find no evidence for a systematic bias relative to the statistical error of the original parameter recovery of GW150914 due to modeling approximations or modeling inaccuracies. However, parameter biases are found to occur for some configurations disfavored by the data of GW150914: for binaries inclined edge-on to the detector over a small range of choices of polarization angles, and also for eccentricities greater than ~ 0.05 . For signals with higher signal-to-noise ratio than GW150914, or in other regions of the binary parameter space (lower masses, larger mass ratios, or higher spins), we expect that systematic errors in current waveform models may impact gravitational-wave measurements, making more accurate models desirable for future observations.

PACS numbers: 04.25.Dg, 04.25.Nx, 04.30.Db, 04.30.Tv

I. INTRODUCTION

We recently reported the first direct observation of a gravitational wave (GW) signal by the Advanced Laser Interferometer Gravitational wave Observatory (aLIGO), from the merger of two black holes, GW150914 [1]. The merger occurred at a distance of ~ 410 Mpc and the black holes were estimated to have masses of $\sim 36 M_\odot$ and $\sim 29 M_\odot$, with spins poorly constrained to be each < 0.7 of their maximum possible values; we discuss the full properties of the source in detail in Refs. [2, 3], subsequently refined in [4]. These parameter estimates relied on three semi-analytic models of binary black hole (BBH) GW signals [5–10]. In this paper we investigate systematic parameter errors that may have resulted from the approximations or physical infidelities of these waveform models, by repeating the analysis of Ref. [2] using a set of numerical relativity (NR) waveforms from configurations similar to those found for GW150914.

The dynamics of two black holes as they follow a non-eccentric orbit, spiral towards each other and merge, are determined by the black hole (BH) masses m_1 and m_2 , and the BH spin angular momenta \mathbf{S}_1 and \mathbf{S}_2 . The resulting GW signal can be decomposed into spin-weighted spherical harmonics, and from these one can calculate the signal one would observe for any orientation of the binary with respect to our detectors. For binary systems where the detectors are sensitive to the signal from only the last few orbits before merger (such as GW150914), we can calculate the theoretical signal from NR solutions of the full nonlinear Einstein equations (see e.g. [11, 12]). However, since the computational cost of NR simulations is substantial, in practice Refs. [2–4] utilized

semi-analytic models that can be evaluated millions of times to measure the source properties.

The models used in the analysis of GW150914, non-precessing EOBNR [5, 6], IMRPhenom [7], and precessing EOBNR [5, 9, 10], estimate the dominant GW harmonics for a range of BBH systems, incorporating information from post-Newtonian (PN) theory for the inspiral, and the effective-one-body (EOB) approach for the entire coalescing process, and inputs from NR simulations [13, 14], which provide a fully general-relativistic prediction of the GW signal from the last orbits and merger. Non-precessing EOBNR represents signals from binaries where the BH-spins are aligned (or anti-aligned) with the direction of the binary's orbital angular momentum¹, $\hat{\mathbf{L}}$. In such systems the orbital plane remains fixed (i.e., $\hat{\mathbf{L}} = \text{const.}$) and the binary is parameterized only by each BH mass and each dimensionless spin-projection onto $\hat{\mathbf{L}}$,

$$\chi_{iL} \equiv \frac{c \mathbf{S}_i \cdot \hat{\mathbf{L}}}{G m_i^2}, \quad (1)$$

where $i = 1, 2$ labels the two black holes, c denotes the speed of light and G Newton's constant.

For binaries with generic BH-spin orientations, the orbital plane no longer remains fixed (i.e., $\hat{\mathbf{L}} \neq \text{const.}$), and such binaries exhibit precession caused by the spin components orthogonal to $\hat{\mathbf{L}}$ [16, 17]. Depending on the orientation of the orbital plane relative to an observer at a reference epoch (time or frequency), the inclination of the binary is defined as

$$\iota := \arccos(\hat{\mathbf{L}} \cdot \hat{\mathbf{N}}), \quad (2)$$

* Full author list given at the end of the article

¹ In this work, we always refer to the Newtonian angular momentum, often denoted L_N in the technical literature [15].

where $\hat{\mathbf{N}}$ denotes the direction of the line-of-sight from the binary to the observer, precession-induced modulations are observed in the GW signal. The waveforms from such binaries are modeled in precessing EOBNR and precessing IMRPhenom. The precessing IMRPhenom waveform model incorporates precession effects through a single precession spin parameter χ_p [18] and one spin-direction within the instantaneous orbital plane. These parameters are designed to capture the dominant precession-effects, which are described through approximate PN results. Precessing EOBNR utilizes an effective-one-body Hamiltonian and radiation-reaction force that includes the full six spin degrees of freedom, which are evolved using Hamilton’s equations of motion. Both precessing models —IMRPhenom and EOBNR— are calibrated only against non-precessing numerical simulations, although both models were compared with precessing numerical simulations [5, 9, 10, 19]. While inclusion of the complete spin-degrees of freedom in the precessing EOBNR models can be advantageous [10], precessing EOBNR suffers the practical limitation of high computational cost. For that reason complete parameter estimation (PE) results using precessing EOBNR for GW150914 were published separately [3], and PE for the two other BBH events reported during the first aLIGO observing run, LVT151012 and GW151226 [4, 20], are presently only available based on non-precessing EOBNR and precessing IMRPhenom. We also restrict this study to non-precessing EOBNR and precessing IMRPhenom but include non-precessing IMRPhenom in select studies.

Apart from the treatment of spin (aligned-spin, effective precession-spin, full-spin), all waveform models discussed include errors due to the limited number of NR calibration waveforms, the inclusion of only the strongest spherical-harmonic modes, and the assumption of a non-eccentric inspiral. Our previous analyses [3, 4, 20] indicated that GW150914 is well within the parameter region over which the models were calibrated, and most likely oriented such that any precession has a weak effect. The goal of the present study is to ensure that our results are not biased by the limitations of the waveform models. We achieve this by performing the parameter recovery on a set of NR waveforms, which are complete calculations of the GW signal that include the full harmonic content of the signal, limited only by small numerical inaccuracies that we show are insignificant in the context of this analysis.

Our analysis is based on injections of numerical waveforms into simulated or actual detector data, i.e. we add gravitational waveforms from NR to the data-stream, and analyze the modified data. We consider a set of NR waveforms as mock GW signals and extract the source properties with the same methods that were used in analyzing GW150914 [2], with two main differences: (1) by injecting NR waveforms as mock signals, we know the exact parameters of the waveform being analyzed. This knowledge allows us to compare the probability density function (PDF) obtained by our blind analysis with the simulated parameters of the source; (2) in order to assess the systematic errors independently of the statistical noise fluctuations, we use the estimated power spectral density (PSD) from actual aLIGO data around the time of GW150914 as the ap-

	injected value	GW150914
signal-to-noise-ratio ρ	25	23.7
f_{ref}	30 Hz	20 Hz
detector-frame total mass	$74.10 M_{\odot}$	$70.6^{+4.6\pm0.5}_{-4.5\pm1.3} M_{\odot}$
inclination ι	162.55°	—
polarisation angle ψ	81.87°	—
right ascension α	$07^h26^m50^s$	—
declination δ	-72.28°	—

TABLE I. Fiducial parameter values chosen for all analyses unless stated otherwise and the corresponding estimates for GW150914. ι denotes the inclination at the reference frequency f_{ref} , ψ the polarization angle and (α, δ) the location of the source in the sky (see Sec. II C for details). The total mass and the four angle parameters are chosen from within the 90% credible intervals obtained in the Bayesian analysis presented in Ref. [2], where the polarization angle was found to be unconstrained, the inclination strongly disfavored to be misaligned with the line-of-sight and results for the sky location are depicted in Fig. 4 therein.

propriate weighting in the inner product between the NR signal and model waveforms. We use injections into “zero noise” where the data is composed of zeros plus the mock signal. This makes our analysis independent of a concrete (random) noise-realization so that our results can be interpreted as an average over many Gaussian noise realizations. The detector noise curve enters only in the power spectral density which impacts the likelihood-function Eq. (14) through the noise-weighted inner product, Eq. (10). This allows us to properly include the characteristics of aLIGO’s noise.

While systematic errors could be assessed from the computation of the fitting factor [21], Bayesian parameter estimation has several advantages: (i) it provides information about the statistical error at the signal-to-noise ratio (SNR) that the signal is seen at in the detector network; (ii) it performs a detailed and robust sampling of the vicinity of the best fit parameters; (iii) it properly includes the response of a detector network; (iv) it replicates the setup of the parameter estimation analyses used for GW150914 and therefore enables immediate comparisons.

We test a variety of binary configurations in the vicinity of GW150914’s parameters. In particular, for several analyses we choose NR configurations² at *fiducial* parameter values consistent with those found for GW150914 [2]. Those fiducial parameter values are listed in Table I in comparison to the parameter estimates for GW150914 [2].

Throughout this paper we will be using two effective spin parameters to represent spin information: First, an effective inspiral spin, χ_{eff} , defined by [22, 23]

$$\chi_{\text{eff}} := \frac{m_1 \chi_{1L} + m_2 \chi_{2L}}{m_1 + m_2}, \quad (3)$$

² Due to the time required to produce NR simulations, these were initiated shortly after the detection of GW150914 when final parameter estimates were not yet available. Thus, our fiducial values differ slightly from the final parameter estimates.

where χ_{iL} is defined in Eq. (1), and, second, an effective precession spin, χ_p , a single spin parameter that captures the dominant spin contribution that drives precession during the inspiral (cf. Eq. (3.4) in Ref. [18]).

We first address the recovery of the binary parameters for aligned-spin systems, and then for precessing ones. Then we study the effect of different polarization angles and inclinations and address the question of the influence of higher harmonics. Since the semi-analytic waveform models only model a quasi-spherical orbital evolution, we also investigate any biases related to residual eccentricity. Finally, we investigate the effects of non-stationary detector noise and numerical errors.

Our study can only determine whether our waveform models would incur a bias in the parameters we have measured, but cannot tell us whether further information could be extracted from the signal, e.g., additional spin information beyond the effective precession parameter in IMRPhenom, or eccentricity. The parameter-estimation analysis of GW150914 with precessing EOBNR provides slightly stronger constraints on the BH spins, but limited additional spin information [3]. No studies have yet been performed to estimate the eccentricity of GW150914, although preliminary investigations have bounded the eccentricity to be ≤ 0.1 [2].

The strategy pursued here—inject known synthetic (NR) signals, recover with waveform models—joins a complementary study that analyses the GW150914-data based directly on numerical waveforms [24] instead of making use of semi-analytic waveform models. In another study [25], additional NR simulations were performed for parameters similar to GW150914. Those, along with other simulations from [25], were compared with the reconstructed signal of GW150914 from unmodelled searches, and provided an independent check on source parameters [26].

The remainder of this paper is organized as follows: In Sec. II we describe the NR waveforms we use as mock GW signals, and summarize the Bayesian PE algorithm, the NR injection framework and the waveform models, which our NR injections are compared against. In Sec. III we present the results of our various analyses. Our main result is that the different waveform models used in the analysis of GW150914 did *not* induce any significant systematic errors in our measurements of this source. We conclude in Sec. IV.

II. METHODOLOGY

A. Waveform models

In this section we briefly describe the waveform models used to measure the properties of GW150914. We summarize the assumptions and approximations behind each model, and highlight their domains of validity in the BBH parameter space. All models aim to represent non-eccentric BBH inspirals. Such binaries are governed by eight source-intrinsic degrees of freedom: The two black hole masses $m_{1,2}$, and the two dimensionless black hole spin-vectors $\chi_{1,2}$. The waveform measured by a GW detector on Earth also depends on extrinsic parameters that describe the relative orientation of

the source to the detector, bringing the total number of degrees of freedom in parameter estimation to 15. Owing to the scale-invariance of vacuum general relativity (GR), the total mass scales out of the problem, and a seven-dimensional intrinsic parameter space remains, which is spanned by the mass-ratio $q \equiv m_2/m_1 \leq 1$, and the spin-vectors. The spatial emission pattern of the emitted GW is captured through spherical harmonic modes (ℓ, m) defined in a suitable coordinate system. All models used here represent only the dominant quadrupolar gravitational-wave emission, corresponding approximately to the $(\ell, m) = (2, \pm 2)$ spherical-harmonic modes.

Two main approaches to construct analytical inspiral-merger-ringdown (IMR) waveform models have been developed in recent years: the EOB formalism and the phenomenological framework.

The EOB approach to modeling the coalescence of compact-object binaries was first introduced in Refs. [27, 28] as a way to extend the PN results of the inspiral to the strong-field regime, and model semi-analytically the merger and ringdown stages. In this approach, the conservative PN dynamics of a pair of BHs is mapped to the motion of a test particle moving in a deformed Kerr spacetime, where the deformation is proportional to the symmetric mass ratio, $\nu = m_1 m_2 / (m_1 + m_2)^2$, of the binary. Prescriptions for resumming PN formulas of the waveform modes are used to construct inspiral-plunge GW signals [29–31]. To improve agreement with NR waveforms, high-order, yet unknown PN terms are inserted in the EOB Hamiltonian and tuned to NR simulations. Also, additional terms are included in the waveform to improve the behavior during plunge and merger (e.g., non-quasi-circular corrections) and to optimize agreement with NR waveforms. The ringdown signal is modeled as a linear combination of quasi-normal modes [32, 33] of the remnant BH. A number of EOB models were developed for non-spinning (e.g. [34, 35]), aligned-spin (e.g. [36, 37]), and generic spin-orientations (i.e., precessing systems, e.g. [9]). They differ mainly by the underlying PN resummation and NR waveforms used to calibrate them. All current EOB models rely on NR simulations [13, 34, 38–42] to achieve a reliable representation of the late inspiral, merger and ringdown portion of the BBH waveforms.

The present study is based on the EOB model of Ref. [5] for aligned-spin BBH, which we shall refer to as non-precessing EOBNR.³ This model was calibrated to NR waveforms with mass ratios between 1 and 1/8, and spins $-0.95 \leq \chi_{iL} \leq 0.98$ for $q = 1$, as well as $-0.5 \leq \chi_{iL} \leq 0.5$ for $q \neq 1$. This waveform model can be evaluated for arbitrary mass ratios and spin magnitudes. While the model can be evaluated outside its calibration region, its accuracy there is less certain than within the calibration region. This model was extensively validated against independent NR simulations [5, 10, 43–46], but the time integration of the EOB equations makes its evaluation computationally expensive. For the comprehensive PE studies presented here, we therefore employ a frequency-domain

³ The technical name of this model in LALSuite is SEOBNRv2.

reduced-order-model (ROM) [6, 47] of the non-precessing EOBNR.⁴ Recently, Ref. [48] introduced several optimizations that have significantly reduced the waveform generation time of the time-domain implementation, although the reduced-order-model remains significantly faster.

The generic-spin precessing time-domain EOBNR model⁵ [9, 10] derives its orbital- and spin-dynamics from the EOB Hamiltonian of Refs. [49, 50], which incorporates all six spin-degrees of freedom. The current precessing EOBNR model directly uses calibration parameters from the non-precessing EOBNR model, without renewed calibration on precessing NR simulations. The ringdown signal is generated in the frame aligned with the spin of the remnant BH as a superposition of quasi-normal modes. The full IMR waveform (as seen in the inertial frame of an observer) is obtained by a time-dependent rotation of the waveform modes in a suitable non-inertial frame, i.e. the precessing-frame [51], according to the motion of the Newtonian angular momentum, and by a constant rotation of the ringdown. An extensive comparison [10] of the precessing EOBNR model to precessing NR simulations with mass ratios $1 \geq q \geq 1/5$ and dimensionless spin magnitudes $cS_i/(Gm_i^2) \leq 0.5$, finds remarkable agreement between them. Extensive code optimizations [48] have also been performed on this model, but unfortunately, its computational cost still prohibits its use in the present study.

The phenomenological approach exclusively focuses on the gravitational waveform without providing a description of the binary dynamics. It is aimed at constructing a closed-form expression of the GW signal in the frequency domain for computational efficiency in GW data analysis. Phenomenological models were first introduced in Refs. [52, 53] to describe the IMR waveforms of non-spinning binaries.

IMRPhenom models are built on a phenomenological ansatz for the frequency-domain amplitude and phase of the IMR signal, commonly an analytic extension of an inspiral description, e.g., from PN theory, through merger and ringdown. The functional form of such an extension is chosen based on inspection of NR simulations, and free coefficients in the ansatz are calibrated against the NR waveforms.

Phenomenological models of the dominant $(\ell, m) = (2, \pm 2)$ multipolar modes of the waveform were constructed for non-spinning and aligned-spin BBH [8, 14, 22, 23, 52, 53]. We refer to the most recent aligned-spin phenomenological waveform model as non-precessing IMRPhenom [8, 14].⁶ Non-precessing IMRPhenom was calibrated against NR waveforms with mass ratios between 1 and 1:18 with $-0.95 \leq \chi_{iL} \leq 0.98$ for $q = 1$, and $-0.85 \leq \chi_{iL} \leq 0.85$ for $q \neq 1$. Non-precessing IMRPhenom is calibrated with respect to an effective spin parameter (cf. Eq. (3)), although information from both BH spins enters through the underlying PN phasing and an alternative spin parameterization in the ringdown. Comparisons with independent NR waveforms indicate [46] that

non-precessing IMRPhenom is an accurate waveform model in the region of parameter space of relevance to GW150914.

For precessing binaries with generic BH spin-directions, a direct phenomenological ansatz for the now seven-dimensional physical parameter space is impractical due to a lack of NR simulations and the complicated precession-induced modulations in the waveforms. This problem is addressed by rotating the waveform-modes of *aligned-spin* BBH systems into precessing waveform-modes via a time-dependent rotation which describes the motion of the orbital plane of the precessing BBH under consideration [7, 54, 55]. In this transformation, χ_{iL} are preserved [55]. The most recent precessing IMRPhenom model [7]⁷ used here makes several additional approximations, in order to arrive at a closed-form frequency domain expression: First, the four in-plane spin components are mapped into one effective in-plane precession spin, χ_p [18], and one azimuthal orientation.⁸ Secondly, the precession of the orbital plane is described with orbit-averaged PN equations for single-spin BBH systems. Finally, the stationary-phase approximation is used to derive the frequency domain expressions for the $(\ell = 2)$ multipolar modes of the waveform in the inertial frame of the observer. Both the PN description and the stationary-phase approximation are carried through merger. The spin of the final black hole is also modified due to the in-plane spins. We stress that the precessing sector of the precessing IMRPhenom model was not calibrated to NR simulations, although comparison with precessing NR simulations indicate promising agreement [19].

The non-precessing models represent the dominant $(\ell = 2, m = \pm 2)$ harmonics of the GW signal to within a mismatch accuracy of $\sim 1\%$ across their respective calibration regions [5, 6, 8] (mismatches are defined in Sec. II C), and to within $\sim 0.5\%$ in the region of parameter space near GW150914; see Ref. [46] for detailed comparisons of both the non-precessing EOBNR and IMRPhenom models. Formally, two models are considered indistinguishable if the mismatch $1 - \mathcal{O}$ between them satisfies $1 - \mathcal{O} < 1/(2\rho^2)$ [56–58], where ρ is the SNR. For signals with $\rho = 25$, this corresponds to a mismatch error better than 0.08%, a bound not reached by the waveform models. However, the indistinguishability criterion is only a sufficient condition, and its violation does not necessarily lead to systematic measurement biases in practice.

The waveform differences may be orthogonal to the physical signal manifold [56]; we are dealing with a multidimensional parameter space and waveform differences may be distributed over many parameters; and the waveform errors for individual cases may be oscillatory and average out in the median while increasing the spread of marginal posterior distributions. This has been illustrated in Ref. [59], and is also exemplified by the results of the present study.

⁴ In LALSuite, this model is denoted by SEOBNRv2_ROM_DoubleSpin.

⁵ In LALSuite this model is denoted by SEOBNRv3.

⁶ In LALSuite this model is denoted as IMRPhenomD.

⁷ In LALSuite this model is denoted by IMRPhenomPv2.

⁸ As a result of this effective spin reduction, the waveform seen by any given detector depends on 13 independent parameters instead of the actual 15 degrees of freedom present in a full description of the source.

B. Numerical relativity waveforms

We use NR waveforms produced by two independent codes, which use completely different analytical and numerical methods, the Spectral Einstein Code (SpEC) [41, 60–62] and the bifunctional adaptive mesh (BAM) code [63, 64].

The BAM code solves the Einstein evolution equations using the Baumgarte-Shapiro-Shibata-Nakamura (BSSN) [65, 66] formulation of the 3+1-decomposed Einstein field equations. The BSSN equations are integrated with a fourth-order finite-difference Runge-Kutta time integrator, with Berger-Oliger time-stepping, along with sixth-order accurate spatial finite differencing, based on the method-of-lines for spatial derivatives. The χ -variation [67] of the moving-puncture method [67, 68] is used, where a new conformal factor defined is $\chi_g = \psi^{-4}$, which is finite at the puncture. The lapse and shift gauge functions are evolved using the 1+log slicing condition and the Gamma-driver shift condition respectively. Conformally flat puncture initial data [69–71] are calculated using the pseudospectral elliptic solver described in [72]. BBH simulations were produced by the BAM code [24, 63, 64] with approximately random initial configurations within the 99% credible region inferred for GW150914 [1]. The current study utilizes three of these simulations, the parameters of which are detailed in Table II, which include all harmonic multipoles up to ($\ell = 5$).

The Spectral Einstein Code (SpEC) [41, 60–62] is a multi-domain, pseudospectral collocation code primarily used for the simulation of compact object binary spacetimes. It is capable of efficiently solving a wide array of hyperbolic and elliptic partial differential equations with high accuracy. Conformally curved initial data [73] is constructed in the extended-conformal-thin-sandwich (XCTS) formalism [74], using the SpEC pseudo-spectral elliptic solver [75]. For evolution, SpEC uses the first order formulation [76] of the generalized harmonic form of Einstein's equations [77, 78] in the damped harmonic gauge [79]. Adaptive mesh refinement ensures to achieve high accuracy and efficiency [80]. Dynamical excision is used to handle black hole singularities [81, 82]. SpEC has been successfully employed to study many aspects of modelling compact object binaries (see e.g [13, 41, 44, 83, 84]). In this study we use waveforms from the SXS public catalog [13, 85], which has seen recent additions of 90 aligned-spin waveforms [86], as well as new simulations targeted by GW150914 [87]. All the SXS simulations have > 24 GW cycles and start below 30 Hz at $74 M_\odot$. The SXS waveforms include all harmonics up to and including ($\ell = 8$). The waveforms are extracted on a series of concentric coordinate spheres of various radii and the data is then extrapolated to null infinity with polynomial extrapolation [88]. For precessing configurations, the drift of the center of mass due to residual initial linear momentum is corrected using the method described in [89] to avoid any spurious mixing of GW modes.

Both codes are described in more detail in Ref. [43]. Their results (along with those from three other codes) were found to be sufficiently accurate and consistent for aLIGO observations of equal-mass nonspinning binaries up to an SNR

of ~ 25 [90], which is similar to the expected configuration of GW150914. A recent study comparing SpEC and another moving-punctures code, LazEv [67], also found excellent agreement (with a mismatch $\lesssim 1 \times 10^{-3}$ for aLIGO design sensitivity) between waveforms for an aligned-spin binary with parameters consistent with GW150914 [91]. Waveforms from the BAM code and SpEC *not* used as mock signals in this study were used in the construction of the EOBNR and IMRPhenom models.

C. Gravitational waveform processing & injection

Gravitational waveforms extracted from NR simulations are commonly decomposed into time-dependent multipolar modes $h_{\ell m}(t)$ in a basis of spherical harmonics $^{-2}Y_{\ell m}$ with spin weight -2 . The two GW polarizations h_+ and h_\times are given in terms of the $h_{\ell m}$ -modes by

$$h_+ - ih_\times = \sum_{\ell, m} h_{\ell m}^{-2} Y_{\ell m}. \quad (4)$$

The numerical simulations provide the modes $h_{\ell m}$ evaluated in the coordinates of the numerical simulation (NR-frame) sampled at times determined by the numerical simulation.

We remove initial spurious radiation from the NR data and align the modes such that the peak of the waveform, defined as $h_{\text{peak}} := \max(\sum_{\ell, m} |h_{\ell, m}|^2)$, occurs at the time $t = 0$. We split each complex mode into separate real-valued amplitude $A_{\ell m}$ and phase $\Phi_{\ell m}$ according to

$$h_{\ell m} = A_{\ell m} \exp(i\Phi_{\ell m}). \quad (5)$$

Next, one-dimensional spline interpolants are constructed (separately on the phase $\Phi_{\ell m}$ and the amplitude $A_{\ell m}$ of each mode $h_{\ell m}$), via a greedy algorithm to reduce the data size to a fraction of its original value while guaranteeing reproducibility of the original NR data to within a tolerance of 10^{-6} [92].

A common convention is to define a stationary source frame which is aligned with the geometry of the binary at a certain reference epoch (detector-frame) as follows: the z -axis is parallel to the orbital angular momentum direction, \hat{L} , and the x -axis is parallel to the line \hat{n} pointing from the less massive body m_2 to the more massive body m_1 . Two angles ι and ϕ then denote the latitude and longitude respectively of the observer in that source frame. The (dimensionless) spins of the two bodies, $\chi_i \equiv cS_i/(Gm_i^2)$, $i = 1, 2$, are also expressed with respect to this stationary source frame:

$$\chi_{ix} = \chi_i^{\text{NR}} \cdot \hat{n}, \quad (6)$$

$$\chi_{iy} = \chi_i^{\text{NR}} \cdot (\hat{L} \times \hat{n}), \quad (7)$$

$$\chi_{iz} = \chi_i^{\text{NR}} \cdot \hat{L}. \quad (8)$$

Given an emission direction determined by the angles (ι, ϕ), (in the detector-frame) a total mass $M = m_1 + m_2$ and a desired sampling rate, the one-dimensional spline interpolants are evaluated at the desired uniform time samples to recover the numerical modes $h_{\ell m}(t)$. The source frame angles (ι, ϕ)

ID	q	χ_1	χ_2	χ_{eff}	χ_p	$M\Omega$	N_{orbits}	e	$1 - \mathcal{O}_{\text{res}}$
SXS:BBH:0307	0.813	(0,0,0.32)	(0,0,-0.58)	-0.0839	0.0	0.01972	12.6	4×10^{-4}	2×10^{-5}
SXS:BBH:0308	0.813	(0.0943, 0.0564, 0.3224)	(0.2663, 0.2134, -0.5761)	-0.0842	0.2629	0.019729	12.5	5×10^{-4}	1.4×10^{-4}
CFUIB0020	0.833	(-0.2594, -0.5393, -0.0458)	(-0.0276, -0.2194, 0.3622)	0.1396	0.5985	0.0276	6.6	3.6×10^{-3}	n/a
CFUIB0012	0.833	(-0.1057, 0.2362, 0.1519)	(0.1269, -0.5130, 0.4139)	0.2710	0.4291	0.0268	7.4	7.7×10^{-3}	n/a
CFUIB0029	0.833	(-0.2800, -0.2896, -0.1334)	(0.3437, 0.2283, 0.0989)	-0.0278	0.4028	0.0268	6.5	3.7×10^{-3}	7.3×10^{-5}
SXS:BBH:0318	0.82	(0,0,0.3300)	(0,0,-0.4399)	-0.0168	0.0	0.020539	14.1	0.0049	8.9×10^{-5}
SXS:BBH:0319	0.82	(0,0,0.3300)	(0,0,-0.4399)	-0.0168	0.0	0.020322	14.3	0.0091	1×10^{-4}
SXS:BBH:0320	0.82	(0,0,0.3300)	(0,0,-0.4399)	-0.0168	0.0	0.021330	13.5	0.013	3.1×10^{-5}
SXS:BBH:0321	0.82	(0,0,0.3299)	(0,0,-0.4399)	-0.0168	0.0	0.018717	15.0	0.029	6.5×10^{-5}
SXS:BBH:0322	0.82	(0,0,0.3301)	(0,0,-0.4399)	-0.0168	0.0	0.019363	15.0	0.038	4.9×10^{-4}
SXS:BBH:0323	0.82	(0,0,0.3300)	(0,0,-0.4400)	-0.0168	0.0	0.018392	14.6	0.070	2.2×10^{-4}
SXS:BBH:0324	0.82	(0,0,0.3299)	(0,0,-0.4400)	-0.0168	0.0	0.017351	13.0	0.13	8.7×10^{-4}

TABLE II. Primary simulations used in this study. Given are mass-ratio q , dimensionless spin-vectors $\chi_{1,2}$, and the corresponding effective aligned-spin parameter χ_{eff} and precession-spin parameter χ_p of the precessing IMRPhenom model. Spin-vectors are specified at the reference epoch where the orbital frequency $M\Omega$ takes the indicated value. The last three columns give the number of orbits from the reference-epoch to merger, the orbital eccentricity at reference-epoch, and an approximate measure of the numerical truncation error respectively (see main text for details).

are transformed into the NR-frame, and Eq. (4) is evaluated to compute the GW polarizations h_+ and h_\times . This procedure is described in [93] and implemented in LAL [94].

The GW data recorded by the aLIGO detectors, h_{resp} , are then obtained by projecting these GW polarizations onto each of the aLIGO detectors via the antenna response functions $F_{+,\times}(\alpha, \delta, \psi)$ as follows:

$$h_{\text{resp}} = F_+(\alpha, \delta, \psi) h_+ + F_\times(\alpha, \delta, \psi) h_\times, \quad (9)$$

where (α, δ) denote the right ascension and declination specifying the position of the GW source in the sky in an Earth-centered coordinate system, and ψ is the polarization angle [95–97].

Most of our analyses focus on NR injections into zero noise, but we also perform injections into calibrated strain data from the aLIGO detectors LIGO-Hanford and LIGO-Livingston using tools in the PyCBC software package [98–101].

For all injections we choose a network SNR of 25 and a low-frequency cut-off $f_{\text{low}} = 30$ Hz. The sampling rate is 16,384 Hz and the waveforms are tapered at the start of the injection. We do not apply a high-pass filter but add segment padding to remove any high-pass corruption.

Our analyses commonly utilize a noise-weighted inner product between two waveforms a and b [102]:

$$(a|b) = 4\text{Re} \int_{f_{\text{low}}}^{f_{\text{high}}} \frac{\tilde{a}(f)\tilde{b}^*(f)}{S_n(f)} df. \quad (10)$$

Here $\tilde{a}(f)$ and $\tilde{b}(f)$ are the Fourier-transforms of the real-valued functions $a(t)$ and $b(t)$, respectively and $*$ denotes complex conjugation. We use a high frequency cutoff of $f_{\text{high}} = 2048$ Hz. To estimate the median PSD $S_n(f)$ used in this inner product, we use 512s of aLIGO data measured adjacent to the coalescence time of GW150914.⁹ The strain

data stretches have previously been calibrated such that the total uncertainty in the magnitude of the recorded strain is less than 10% and less than 10° in phase between 20 Hz and 1 kHz [103].

D. Parameters of numerical simulations

Table II lists the parameters of the primary numerical simulations used in this study, whereas Table III summarizes additional simulations that were employed for consistency checks in a wider region of parameter space. The simulations shown in Table II were specifically produced to follow-up GW150914.

For each simulation, parameters are given at the start of the useable numerical simulation, i.e. the reference epoch, indicated by a dimensionless (total mass invariant) orbital frequency $M\Omega$. This dimensionless orbital frequency $M\Omega$ translates into a gravitational-wave starting frequency of

$$f_{\text{GW}} = \frac{M\Omega}{\pi} (GMc^3)^{-1}, \quad (11)$$

for the dominant (2, 2)-harmonic. For $M = 74 M_\odot$, this corresponds to a frequency of $f_{\text{GW}} = M\Omega \times 870$ Hz, so that dimensionless orbital frequencies $M\Omega$ of 0.027 and 0.020 translate to GW frequencies of 23.5 Hz, 17.4 Hz, respectively.

Table II specifies the two dimensionless spin vectors χ_i in the LIGO-frame following Eqs. (6)–(8). The orbital eccentricity e (at reference epoch) is estimated as follows: For the quasi-circular SXS simulations (SXS:BBH:0307, SXS:BBH:0308 and Table III), a sinusoid is fitted to the time-derivative of the orbital frequency as detailed in [104]. For the CFUIB simulations, the eccentricity is measured with reference to an estimate of the non-eccentric frequency evolution, which is found by fitting a fourth-order polynomial to the orbital frequency as in Ref. [105]. More precise estimates of the eccentricity can be made (for non-precessing signals)

⁹ The PSD is generated from an earlier calibration of the data but we have verified that it is accurate to within 1% with a PSD from the final calibration of the data.

from the GW signal, and these can be used to calculate initial parameters for configurations with yet lower eccentricity, but we do not expect such low eccentricities to be necessary for this study [106]; that expectation is supported by the results in Sec. III D. Eccentric binaries exhibit a more complicated behavior of the orbital frequency. For the eccentric simulations (SXS:BBH:0318 to SXS:BBH:0324), therefore, we proceed as follows: the GW frequency is fitted according to Eqs. (16)–(18), and the column “ $M\Omega$ ” in Table II reports the *mean-motion* Mn , cf. Eq. (17), at the reference epoch. Furthermore, for these eccentric simulations, the eccentricity is reported at the same frequency $Mn = 0.0272712$ for all simulations, corresponding to a (2,2) GW frequency of $f_{\text{GW}} = 23.8$ Hz. This decouples the value of the eccentricity from the individual starting frequency of each eccentric simulation (recall that orbital eccentricity decays during the inspiral [107]).

The final column of Tables II and III indicates the numerical truncation error of the simulations computed as follows. For each NR simulation, we take the two waveforms with the highest resolutions at an inclination of $\iota = \pi/3$ and compute the noise-weighted inner product between them. More precisely, we follow the approach of Refs. [10, 108] by considering the notion of the min-max overlap that gives the lowest overlap when considering all sky positions and polarizations.

Specifically, given a waveform of one resolution, h_1 , evaluated at a fixed set of parameters, we choose the polarization angle and sky location of the other resolution h_2 , such that the overlap given by

$$O(h_1, h_2) := \frac{(h_1 | h_2)}{\sqrt{(h_1 | h_1)(h_2 | h_2)}} \quad (12)$$

between the waveforms of the two numerical resolutions is maximized, where the inner product $(\cdot | \cdot)$ is defined in Eq. (10). In addition, we also maximize the overlap over a time- and phase-shift between the two waveforms. We then minimize the overlap over the sky location and polarization of h_1 . By construction, the overlap will always be equal to or above the min-max, regardless of the source parameters, thus making it a suitable conservative measure. An overlap of $O = 1$ indicates perfect agreement between two waveforms. The deviation of the overlap from one, $1 - O$, is referred to as *mismatch*, and is a useful measure to approximately quantify the accuracy of waveforms.

This quantity is averaged over several azimuthal angles and is reported in the last column as $1 - O_{\text{res}}$ in Tables II and III.

In the Fisher-matrix approximation for the single-detector case, two waveforms are considered indistinguishable if their mismatch satisfies $1 - O \lesssim 1/(2\rho^2)$ [56–58]. For $\rho = 25$, this implies that errors in the numerical waveforms will be irrelevant if they lead to mismatches $\lesssim 8 \times 10^{-4}$. For the numerical truncation error (as considered in the column $1 - O_{\text{res}}$ in Tables II and III), we find that this is the case for the numerical simulations considered here. For the SXS waveforms, a detailed analysis of other sources of errors in the numerical simulations finds that other sources of error dominate over numerical truncation error, most notably ambiguities in gravitational-wave extraction, however, the combined error still leads to mismatches $\lesssim 3 \times 10^{-4}$. Therefore, we con-

clude that the SXS simulations are sufficiently accurate for the present study, a conclusion also confirmed in Sec. III F below.

E. Bayesian parameter estimation

The *posterior probability density function* (PDF) of a set of parameters θ which describe the physical properties and orientation of the binary system can be expressed with Bayes’ theorem [109, 110],

$$p(\theta | d, H) = \frac{p(\theta | H) \Lambda(d | \theta, H)}{\int p(\theta | H) \Lambda(d | \theta, H) d\theta}, \quad (13)$$

where $p(\theta | H)$ is the *prior probability density* for θ given a model H and $\Lambda(d | \theta, H)$ is the *likelihood* function. In the case of GW data, the data d is described by the signal $h(\theta_0)$ with given parameters θ_0 and the instrument noise n . The likelihood function can then be written as [102, 111]

$$\Lambda(d | \theta) \propto \exp\left(-\frac{1}{2} (h(\theta) - d | h(\theta) - d)\right), \quad (14)$$

where the notation $(a | b)$ indicates the noise-weighted inner product, cf. Eq. (10).

In order to measure the recovered distribution of the binary system properties, we inject the waveform with the given set of parameters into the data, and use two independent stochastic samplers, based on parallel-tempered Markov-Chain Monte Carlo (MCMC) and on nested sampling algorithms. Our set-up is consistent with [2], and the engine implementations are available in the LALInference package [111] of the LIGO Algorithm Library (LAL) software suite [94].

The samplers are specially designed for GW data analysis, and as well as generating posterior samples for the waveform parameters, they are also capable of marginalizing over uncertainties in the posteriors propagated from the uncertainties in the model used to calibrate GW strain data [112]. The marginalization assumes that errors in the phase and amplitude of the data can be fit with a spline model consisting of ~ 5 points placed at intervals in the frequency domain [2, 113].

To represent the full joint distribution of the parameters would be unfeasible, so instead, we present posteriors marginalized in all but one or two dimensions: the width of these posteriors (often encoded in a confidence interval) encodes the statistical uncertainty in the measurement. However, it is important to note that many of the parameters have correlated probability densities (e.g., distance/inclination, component masses).

For the most part of this study we do not include noise in the simulated data in order to focus on comparing systematic against statistical errors in an idealized setting. If a waveform model were a perfect match for an NR signal, then the noise-free analysis should yield a posterior PDF peaked at the true parameter values up to biases induced by the priors.

Including detector noise as in the analysis presented in Sec. III E will smear out and shift the posteriors and allow

us to get a sense of realistic statistical uncertainties. The presence of noise will also reduce the impact of systematic biases inherent in waveform models and therefore the noise-free analysis should be conservative.

III. RESULTS

GW150914 has been shown to be consistent with a range of source parameters [2–4], and below we shall show how reliably the methods and waveform models described here can extract the properties of signals that are consistent with the parameter estimates of GW150914. We first analyze non-precessing signals and confirm that all models give reliable results, as expected from their tuning to non-precessing NR simulations [8, 14, 36, 45], and the comparatively small amplitude of higher harmonics for almost equal mass ratios, spins and orientations. In Sec. III B, we turn to precessing signals. Generally, we find no significant parameter biases except for particular choices of polarization angle and source inclination. We discuss this effect in more detail, and demonstrate that systematic biases would be significant for only a small fraction of possible source orientations, and we can confidently conclude that the analysis of GW150914 did not suffer from these biases.

A. Non-precessing binaries

We first study the parameter recovery for NR waveforms with BH spins aligned with the orbital angular momentum direction \hat{L} of the binary. The physical effect of aligned (anti-aligned) spins is to increase (decrease) the number of orbits accumulated from a reference frequency to merger relative to a non-spinning binary. We inject a number of aligned-spin NR waveforms into zero noise and use non-precessing EOBNR [5, 6] and non-precessing IMRPhenom waveforms [8] to estimate the source parameters.

Fig. 1 shows marginalized posterior PDFs for the spin and mass parameters for both waveform models for the NR signal SXS:BBH:0307 with intrinsic parameters as listed in Table II and fiducial parameters listed in Table I. We find that the true parameter values lie well within the 90% credible intervals for either model for these fiducial values. Below we quote the medians, 90% credible intervals and an estimate for the 90% range of the systematic error determined from the variance between the two waveform models. As is expected from earlier theoretical studies [46, 114], and consistent with previous LVC studies of GW150914, we find excellent agreement in the chirp mass, given by

$$\mathcal{M} = \frac{(m_1 m_2)^{3/5}}{M^{1/5}}, \quad (15)$$

which is the coefficient of the leading-order term in the PN phase evolution, while the mass ratio q is broadly consistent with the injected value. For the heavy BBH systems considered here the total mass of the binary is similarly well constrained as the chirp mass [115, 116] due to the dependence

of the ringdown on the total mass [32]. The difference in the location of the peaks in the PDF for the component masses (left panel of Fig. 1) is due to small differences between the two waveform models. For the source frame masses¹⁰ we find $m_1^{\text{source}} = 37.8^{+5.8 \pm 1.6}_{-4.5 \pm 0.5} M_\odot$ and $m_2^{\text{source}} = 29.2^{+4.6 \pm 0.7}_{-5.0 \pm 0.9} M_\odot$, and see that the systematic errors are about a factor 5 smaller than the statistical errors. The effective spin recovery is consistent between the two models, $\chi_{\text{eff}} = -0.11^{+0.14 \pm 0.01}_{-0.15 \pm 0.04}$. However, an anti-symmetric combination of the two spins is not well constrained, indicating the difficulty in measuring the difference between the two spins [118], $(m_1 \chi_{1L} - m_2 \chi_{2L})/M = 0.29^{+0.43 \pm 0.05}_{-1.02 \pm 0.16}$. We note that EOBNR leads to a markedly more pronounced peak of the anti-symmetric $(m_1 \chi_{1L} - m_2 \chi_{2L})/M$ posterior. The EOBNR model incorporates both spins χ_{1L}, χ_{2L} , whereas IMRPhenom primarily utilizes the effective spin χ_{eff} . Therefore, the improved recovery of the anti-symmetric spin combination with EOBNR points to some extra power afforded by the more complete model. However, this improved recovery is not a generic feature found in other configurations and seems to be a spurious effect. This is supported by Ref. [46] who find a mismatch of $\sim 3\%$ for non-precessing EOBNR for configurations with highly anti-symmetric spins at equal-mass. In addition, our analysis uses idealized assumptions of injections into zero-noise, while PE analyses in non-Gaussian detector noise and marginalization over calibration errors would wash out such fine features and their extraction would require SNRs much higher than 25.

In addition, we performed injection and parameter-recovery for a large number of non-precessing-binary signals listed in Table III with similar results, as summarized in Table IV in Appendix A. In summary, we recover parameters that are statistically consistent between the EOBNR and IMRPhenom models, and with those describing the mock NR source. These results confirm previous studies [8, 46].

B. Precessing binaries

1. Fiducial inclination and polarization

GW150914 is consistent with a wide range of BH spin configurations, including the possibility that one or both BH spins are misaligned with the orbital angular momentum. Such misalignments give rise to precession of the BH spins and the orbital plane of the binary, leading to modulations in the gravitational waveform [16, 17]. We now explore the parameter recovery of such precessing sources.

First, we analyze precessing NR signals injected with the fiducial parameters listed in Table I. While the inclination ι is time-dependent for precessing binaries, the orientation of the total orbital angular momentum \mathbf{J} remains almost constant.¹¹

¹⁰ We measure redshifted masses m , which are related to source-frame masses using the relation $m = (1+z)m^{\text{source}}$ [117], where z is the cosmological redshift.

¹¹ The exception to this are binaries that undergo transitional precession [16].

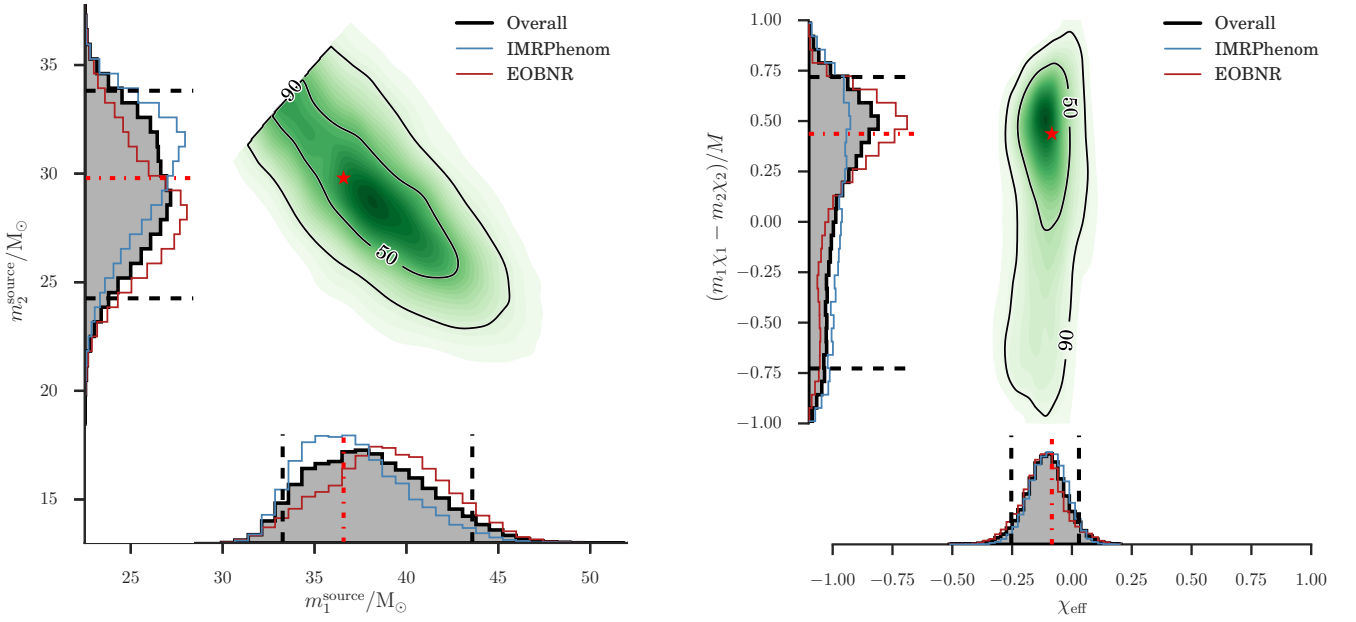


FIG. 1. Comparison of source frame component masses and aligned spin combinations for an aligned NR mock signal (SXS:BBH:0307) with masses and spins consistent with GW150914. The signal is injected into zero noise using the fiducial inclination, $\iota = 163^\circ$, and polarization angle $\psi = 82^\circ$. The non-precessing IMRPhenom and EOBNR models are used for recovery. The left panel shows credible regions for recovery of the component masses, whereas the right panel shows spin recovery. As in [2] we combine the posterior samples of both models with equal weight, in effect marginalizing over our choice of waveform model. The resulting posterior is shown in the two-dimensional plot as the contours of the 50% and 90% credible regions plotted over a color-coded PDF. Dashed lines in the one-dimensional plots show 90% credible intervals of the individual and combined posteriors. The injected parameter values are shown as red dot-dashed lines and a red asterisk. Both models recover the correct masses and effective spin χ_{eff} within the 90% credible regions, while the anti-symmetric spin combination is not measured well; the peak in the EOBNR PDF around the correct value is a spurious effect (see text).

It is therefore often more meaningful to consider the angle θ_{JN} between $\hat{\mathbf{J}}$ and the line-of-sight $\hat{\mathbf{N}}$ instead. We note that for the precessing binaries discussed in this study the opening angle of the precession cone of $\hat{\mathbf{L}}$ around $\hat{\mathbf{J}}$ is only a few degrees at 30 Hz and thus θ_{JN} and ι are close.

As in the original analysis of the properties of GW150914 in Ref. [2], we use the non-precessing EOBNR and precessing IMRPhenom waveform models in this study. Analyses with the precessing EOBNR model are currently not computationally feasible to perform detailed investigations. A comparison between the two precessing models in the estimation of the properties of GW150914 and against two NR injections is discussed in Ref. [3]. It found that the two precessing models showed good agreement in the recovery of both injections.

For this first study we choose CFUIB0029 (see Table II), a simulation where the BH spins point predominantly in the orbital plane, and with a reasonably large value of $\chi_p \approx 0.4$. We inject this waveform at fiducial parameters into zero noise. Figs. 2 and 3 summarize the parameter recovery for this injection. We find that the true parameter values of the NR signal (red asterisks) lie within the 50% credible regions for component masses and effective spins indicating unbiased parameter recovery for this injection with either waveform model. For the source frame masses we find $m_1^{\text{source}} = 38.3^{+6.4}_{-4.9} M_\odot$ and $m_2^{\text{source}} = 28.2^{+5.3}_{-6.2} M_\odot$, with systematic errors an order of magnitude smaller than statistical errors. For the effective aligned spin we have $\chi_{\text{eff}} = -0.08^{+0.15}_{-0.19}$. Here systematic

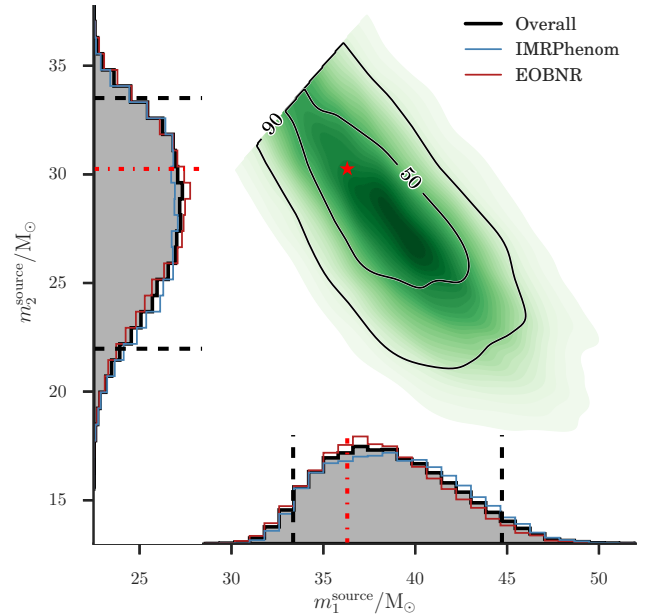


FIG. 2. Comparison of component masses for a precessing NR mock signal (CFUIB0029) with masses and spins consistent with GW150914. The mock signal is injected in zero noise using the fiducial inclination, $\iota = 163^\circ$, and polarization angle $\psi = 82^\circ$. The precessing IMRPhenom and non-precessing EOBNR models are used for recovery.

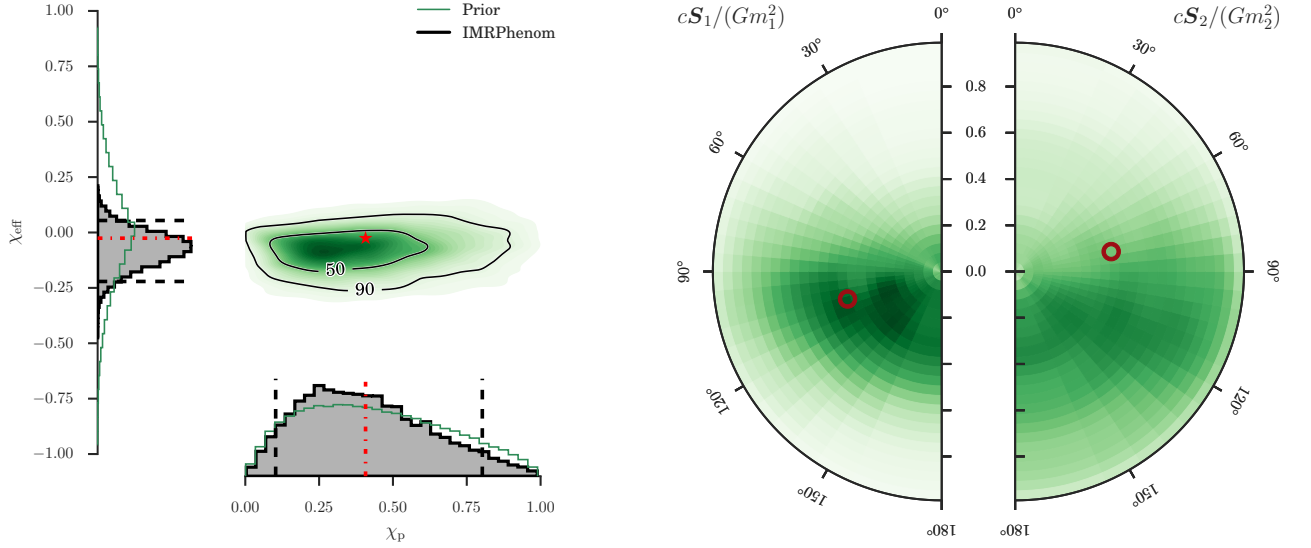


FIG. 3. Comparison of spins for the precessing NR mock signal (CFUIB0029) shown in Fig. 2. Left: PDFs for the χ_p and χ_{eff} spin parameters. The one-dimensional plots show probability contours of the prior (green) and marginalized PDF (black). The dashed vertical lines mark 90% credible intervals. The two-dimensional plot shows the contours of the 50% and 90% credible regions plotted over a color-coded PDF. The injected parameter values are shown as red dot-dashed lines and a red asterisk. Right: PDFs for the dimensionless component spins $cS_1/(Gm_1^2)$ and $cS_2/(Gm_2^2)$ relative to the normal to the orbital plane \mathbf{L} , marginalized over uncertainties in the azimuthal angles.

errors are a factor four smaller than statistical errors. The absolute bias between the true parameter values and the overall medians in the source frame masses is $\approx 2M_\odot$ and ≈ 0.05 in χ_{eff} . The spin directions as shown in the right panel of Fig. 3 are not constrained. No information on the effective precession spin χ_p is recovered, despite the signal having appreciable χ_p . Instead, we effectively recover the prior on χ_p as can be seen in the left panel of Fig. 3. This may be attributed to the following reasons: Firstly, the fiducial inclination only gives rise to weak precession-induced modulations in the signal, and secondly the shortness of the signal only allows for at most one modulation cycle in the aLIGO sensitivity window. Hence we find that for the fiducial parameters, parameter recovery is *not biased* in the sense that the injected values are always well inside their posterior confidence regions.

Parameter estimates were obtained for several additional NR signals in the vicinity of GW150914 with the precessing IMRPhenom model for fiducial and also edge-on inclinations of the source. The results are summarized in Table V in Appendix A. These results agree with the findings in this section that parameter recovery is not biased for the fiducial parameters. On the other hand, if the source is viewed at nearly edge-on, inclination biases can arise and we will discuss these next in Sec. III B 2. We note that for some configurations we find small disagreements in the shapes of the PDFs, similar to those found for the non-precessing injection in Fig. 1. However, these differences do not noticeably affect the credible intervals, and we find no clear relationship between the level of disagreement and the location in parameter space.

2. Varying inclination and polarization

In Sec. III B 1 we found that the IMRPhenom and EOBNR models recover the injected parameters with comparable accuracy as expected from the results of GW150914, without significant bias. However, precession-induced signal modulations become stronger for sources viewed at an angle of $\theta_{\text{JN}} \sim 90^\circ$ (edge-on) (see e.g. [16, 55, 119]). For such orientations two qualitatively new features arise in the waveform: the circular orbital motion becomes approximately linear when observed edge-on, thus preferring the observation of the plus polarization, while the precession of the orbital plane dominates the other polarization. Signals from such sources have a richer waveform structure and are more challenging to capture by the models discussed here. When injecting and recovering precessing waveforms edge-on, we find: (1) PE may yield biased results with the level of bias depending on both the source inclination *and* signal polarization; (2) the bias is most likely caused by discrepancies between precessing IMRPhenom and the fully general-relativistic NR signals, but (3) these biases only manifest themselves for certain source orientations and polarizations, and as such are likely to constitute only a small fraction of observations.

The inclination ι of the source relative to the detector strongly affects the morphology of the detected signal. In addition, the signal recorded at the detector also depends on the polarization angle ψ as well as the position in the sky (α, δ) (cf. Eq. (9)). For the current two-detector network, which is principally sensitive to only one GW polarization for any given sky location, this suggests that ψ , α and δ may be partially degenerate, as supported by Refs. [120, 121]. Therefore, we expect that varying ψ , while fixing the sky position, will lead to an effective exploration of the extrinsic param-

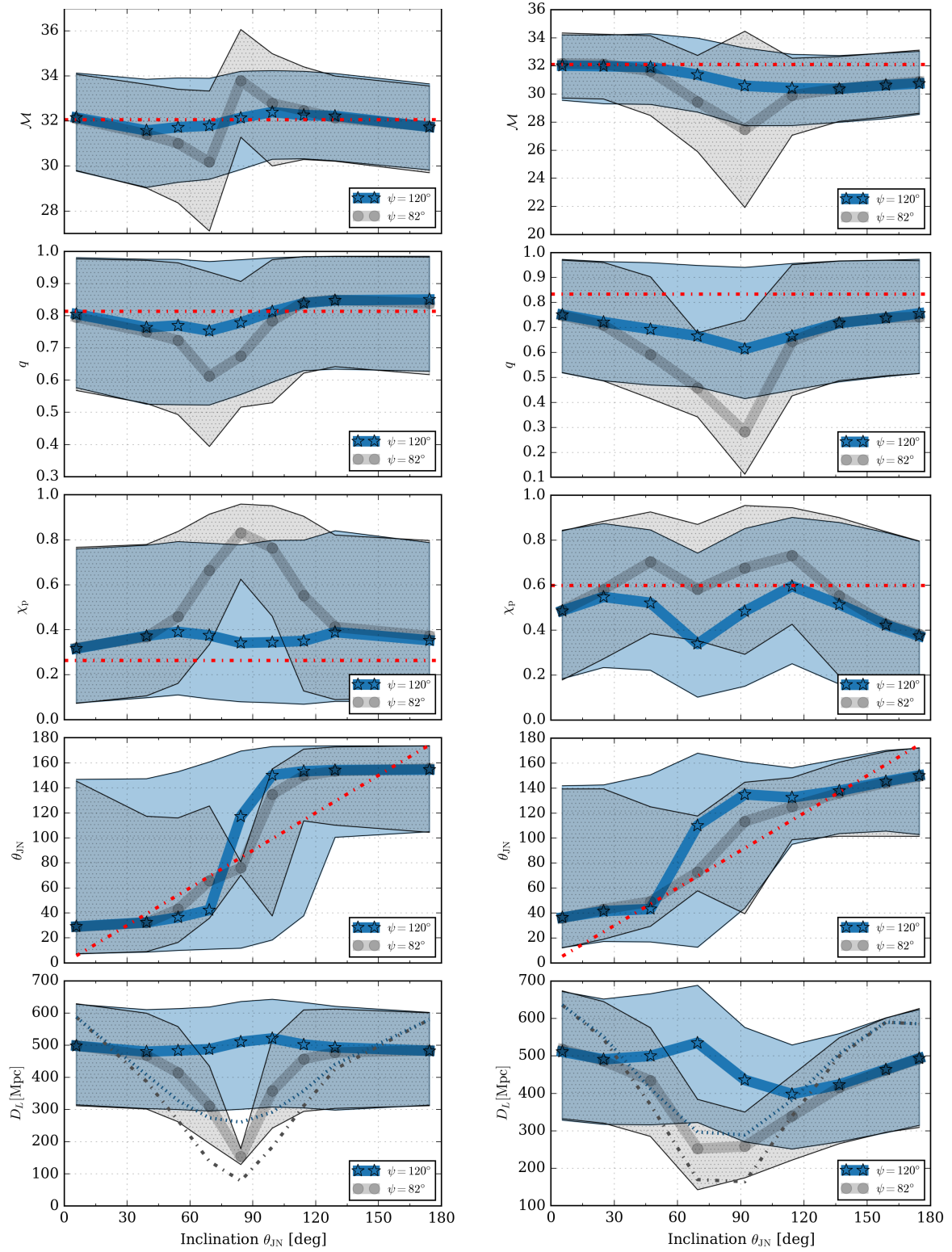


FIG. 4. Inclination dependence of parameter recovery. Two NR waveforms primarily differing in χ_p (SXS:BBH:0308 in left column; CFUIB0020 in right column) are injected with different θ_{JN} as given on the ordinate axes. Shown on the abscissa axes are 90% credible intervals (blue / gray bands) and medians (asterisks / circles) for these precessing NR signals recovered with the precessing IMRPhenom model. Injected parameter values are shown as red dash-dotted lines, except for the bottom two panels where the injected values depend on ψ and are shown in blue (dotted) and gray (dash-dotted). Shown from top to bottom are chirp mass \mathcal{M} , mass-ratio q , effective precession spin χ_p , the angle θ_{JN} and luminosity distance D_L . The analysis is repeated for two choices of detector polarization angle ψ , with the one shown in grey representing a detector orientation approximately canceling h_+ .

ter space. In this context, we assess how well the precessing IMRPhenom waveform model approximates GW signals when varying amounts of h_+ and h_\times polarization are present at different inclinations.

We focus our investigation on four NR simulations: CFUIB0029, CFUIB0012 and CFUIB0020, and SXS:BBH:0308 as listed in Table II. We find the results to be qualitatively consistent between all four cases, and in what follows we focus on CFUIB0020 and SXS:BBH:0308, as examples of waveforms from two independent NR codes. NR injections were again performed into zero noise with the fiducial parameter given in Table I but with varying inclination and polarization angles. An overview of our results is given in Fig. 4. We find that:

- Results are qualitatively similar between simulations (CFUIB0020 and SXS:BBH:0308) for two different choices of physical BBH parameters.
- Parameter estimates with IMRPhenom are most accurate for signals with inclinations near 0° (“face-on”) or 180° (“face-off”).
- Results depend on the polarization angle when signals have an inclination near 90° .
- For inclinations and polarization angles in a region near 90° , recovered parameter values (e.g., for mass ratio) deviate most strongly from injected parameters. In rare cases, the injected parameters lie outside the 90% credible region.

While Fig. 4 demonstrates qualitatively similar results for the parameter recovery of the SpEC and the BAM simulations, we note two differences for near edge-on inclination at $\psi = 82^\circ$: For SXS:BBH:0308 (left column) the recovered distance is overestimated, correlated with a significantly overestimated χ_p , while the other parameters show no large biases. For CFUIB0020 (right column), on the other hand, the mass ratio q shows a significant bias. We find that both χ_p and q are correlated with extrinsic parameters. Depending on details of the NR signal, either one can be heavily biased. We further point out that for this orientation and polarization: (a) The distance prior (strongly) and the likelihood (less strongly) favor a source-distance larger than the injected distance. (b) The posterior samples show systematic biases: Those samples near the actual injected distance correlate with less biased values of χ_p and q than posterior samples that have a larger distance. (c) The recovered sky position (α, δ) is strongly biased. (d) The recovered SNR is only 23 (for the injection at SNR of 25).

Conversely, we see no biases when the source polarization matches the dominant polarisation frame (DPF) [122, 123] of the network, for $\psi \sim 120^\circ$, (i.e., when the network has maximum response to the source-frame h_+ and minimum response to the source-frame h_\times). However, we see clear biases when the source polarization is near 45° to the DPF (i.e., when the network has maximum response to the source-frame h_\times and minimum response to the source-frame h_+) as described above.

We can see that this is indeed the case by considering the time-domain waveforms for cases with and without observed parameter biases. Fig. 5 shows the detector response h_{resp} and the incident GW polarizations, h_+ and h_\times , for LIGO-Hanford and LIGO-Livingston for CFUIB0020 viewed edge-on with $\theta_{\text{JN}} = 92^\circ$. The components h_+ and h_\times are the same on the left and right panels, but the proportion of each polarization that contributes to the signal h_{resp} differs. The left panels show the complete signal for a polarization angle $\psi = 120^\circ$, and the right panels show the complete signal for a polarization angle $\psi = 82^\circ$. We see that for $\psi = 120^\circ$ the observed signal is dominated by h_+ , whereas in the right panels the observed signal is dominated by h_\times .

In particular, we see that for a given polarization angle and source inclination, the detector response may correspond to the partially constructive or destructive interference of h_+ and h_\times , which amplifies or diminishes the observed signal. Such cases are especially challenging and require waveform models that describe $h_{+,\times}$ very accurately. However, in the construction of the precessing IMRPhenom only the aligned-spin ($2, \pm 2$)-modes are used. By construction, the neglect of higher-order aligned-spin modes results in approximate precessing modes. This approximation becomes more inaccurate for systems close to edge-on, as contributions from higher-order modes to the observed signal become more important. In addition, for a suitable polarization angle ψ , the ($2, \pm 2$)-contributions to the signal may vanish completely and any observed strain at the detector arises purely from higher-order waveform modes. Since such modes are not accurately described by the precessing IMRPhenom model but are contained in our NR signals, we attribute the observed bias and reduction in recovered SNR to the incompleteness of the model.

To confirm this, we have injected signals generated with the precessing IMRPhenom model, and performed PE recovery with this same model. This test shows no appreciable biases in the recovered parameters. This suggests that in these cases, other possible sources of bias (for example, due to the choice of priors in the Bayesian analysis) did not have a significant impact on the results. Another possibility is that the biases are caused by inaccuracies in the NR waveforms, but since we see similar effects between waveforms calculated from both the BAM code and SpEC, we consider this unlikely. We therefore conclude that the PE biases for the configurations with $\theta_{\text{JN}} \approx 90^\circ$ in Fig. 4 indeed arise from a lack of fidelity between the waveform model and the full NR signals.

With this in mind, a practical question becomes *what fraction of future detections will incur such biases?* Unfortunately, without knowledge of the mass distribution of future observations, and given the small sample of configurations analyzed here, we cannot answer this question in full generality.

However, our investigation demonstrates that large parameter biases occur only in strongly inclined binaries. For these orientations, the observed GW signal is weaker than for other orientations, which significantly reduces their detectability. As an illustration, we can estimate that only 0.3% of observable sources will fall into a $30^\circ \times 30^\circ$ region in inclination and polarization around the point of minimal amplitude (which we take approximately as the point of maximal bias). Details of

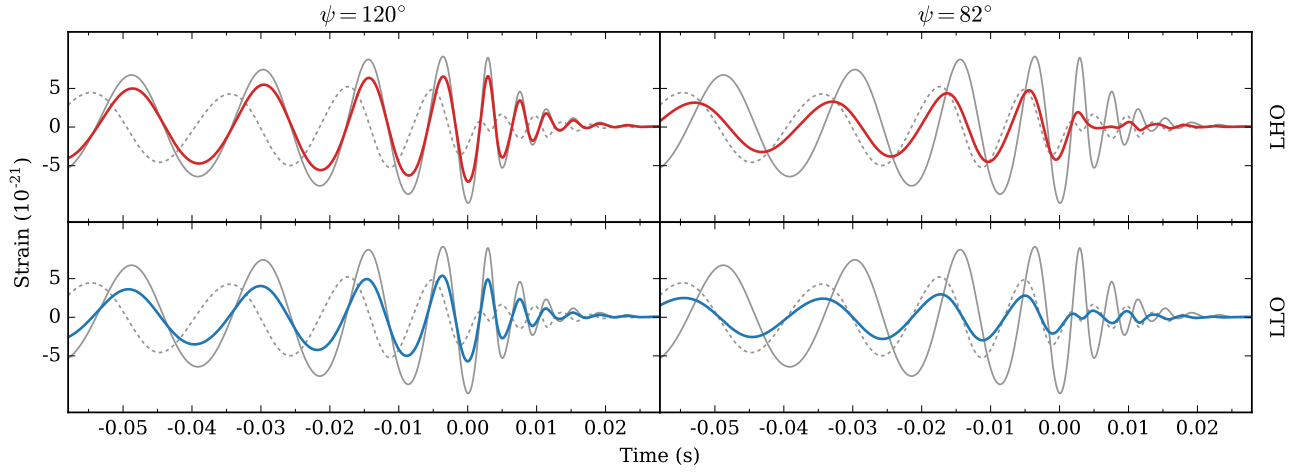


FIG. 5. Comparison of detector responses using NR waveform CFUIB0020 at an angle $\theta_N = 92^\circ$. Incoming h_+ and h_\times polarizations are shown by grey solid and dashed curves respectively. The left column shows the theoretical detector response (Eq. (9)) in red for LHO on the top row and in blue for LLO on the bottom row, for a polarization angle of $\psi = 120^\circ$. The right column shows the responses for a polarization angle of $\psi = 82^\circ$. In both cases the distance to the source is 40 Mpc. The signal at LHO has been inverted to account for the relative detector orientations, and the signals are aligned in time; cf. Fig. 1 in [1]. We find significant differences in the detector responses between the two polarization angles (see text for details).

this calculation are presented in Appendix B.

C. Higher modes

IMR waveform models for spinning BBH with higher modes are not yet available. Our analysis uses the precessing IMRPhenom waveform model which includes only spherical harmonics of multipole $\ell = 2$. In Secs. III A and III B we have analyzed parameter recovery of complete NR signals containing higher modes up to multipole $\ell = 8$, although, since the GW frequency scales with m , harmonics with $m \geq 3$ turn on within the detector band because of the limited length of the NR waveforms.

Higher modes are likely unimportant for nearly equal-mass systems and become more relevant as the mass ratio decreases [35, 124–127]. The importance of higher modes also increases with the total mass of the system as the merger part of the signal moves into the most sensitive part of the aLIGO band. Because no recovery waveform families exist which incorporate higher modes, we test their importance by changing the injected waveform: Starting from the precessing simulation SXS:BBH:0308 (see Table II), we inject (a) the full NR waveform with all modes up to $\ell = 8$. And (b) a “truncated” NR waveform that consists only of the $\ell = 2$ modes. All injections are recovered with precessing IMRPhenom templates.

Our results are summarized in Fig. 6. When the binary is viewed face-on there is very good agreement in the posteriors irrespective of whether the NR mock signal includes all higher harmonics or just the $\ell = 2$ modes and the posteriors peak close to the true parameter values. However, when viewed from edge-on inclination, parameter recovery is biased. The larger mass m_1 is somewhat overestimated, and the effective precession spin parameter is significantly overesti-

mated, indicating erroneously a nearly maximally precessing system, with the actual injected χ_p far outside the recovered 90% credible region. These biases arise for both the full NR waveform, $\ell \leq 8$, and “truncated” NR waveform, $\ell = 2$. At edge-on inclination the higher harmonics contribute more to the GW signal and their inclusion or absence also influences parameter recovery. But this effect is much smaller than the bias arising from the inclination of the signal.

We can refine the conclusions of Sec. III B and say that the precessing IMRPhenom waveform model leads to biased parameter recovery for only a very small fraction of orientations in the vicinity of GW150914, namely when the system is viewed close to edge-on and if the GW polarization happens to be unfavorable. For these exceptional cases we find that most of the modeling error stems from the $\ell = 2$ modes while neglecting modes with $\ell > 2$ in the model only causes additional small modeling errors. See [24] for a more detailed discussion of cases where higher modes can provide additional information.

To further quantify the effect of higher modes, we compute the mismatch between the NR waveforms including only $\ell = 2$ modes and those including all modes up to $\ell = 8$. The computation is done in the same way as in Tables II and III using the highest available resolution. We find that the typical mismatches for configurations with mass-ratios and spins compatible with GW150914 (such as SXS:BBH:0308, SXS:BBH:310) are of order few $\times 10^{-3}$, rising to few $\times 10^{-2}$ for configurations with high spin (e.g. SXS:BBH:0233, SXS:BBH:0257, SXS:BBH:0531) and become the largest (~ 0.1) for mass ratio $q = 0.125$ (SXS:BBH:0065). The mismatches are also higher for higher inclinations, becoming largest for edge-on configurations.

The mismatch at high mass ratio is considerably larger than the fiducial limit from a Fisher argument, consistent with pre-

vious studies that found that subdominant modes become increasingly important for higher mass ratio [124–128]. The Fisher matrix criterion is conservative, and violating it means that explicit PE studies must be performed to assess the effects of neglecting higher modes (see Appendix A for additional NR injections using the fiducial extrinsic parameters). While we do not find significant biases for the cases and parameters considered in this work, we expect that higher modes will become important with larger inclinations and mass ratios.

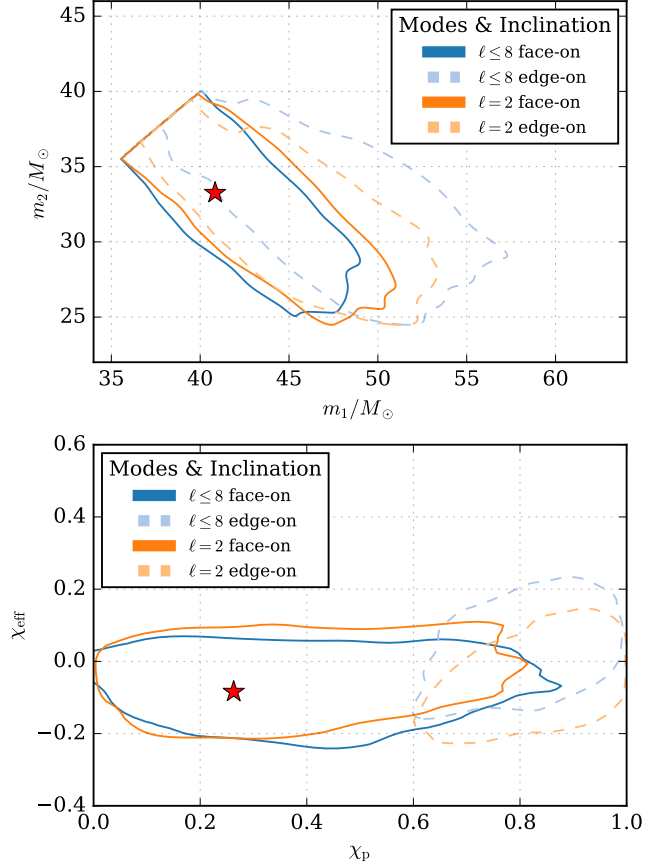


FIG. 6. Results for precessing NR injections (SXS:BBH:0308) with face-on or edge-on inclination ($\theta_{\text{IN}} = 6^\circ$ and 84° , respectively) and either including higher harmonics up to $\ell = 8$ (compare with Fig. 4) or just the $\ell = 2$ modes in the mock signal. All injections are performed at fiducial polarization angle $\psi = 82^\circ$. The precessing IMR-Phenom model is used as the template waveform. We show two-dimensional 90% credible regions for component masses and effective spins.

D. Eccentricity

Since IMR waveform models including spin and eccentricity are not currently available, we assess the effect of eccentricity on PE by injecting NR waveforms of varying eccentricity and studying PE using a non-eccentric waveform model.

We use a family of NR waveforms produced with SpEC with spins aligned with the orbital angular momentum with

mass-ratio $q = 0.82$, and aligned component spins $\chi_{1L} = 0.33$, $\chi_{2L} = -0.44$, a configuration comparable to the parameters of GW150914. The waveforms in this family vary in their orbital eccentricity, cf. Table II.

There is no unambiguous GR definition of eccentricity, so we calculate an eccentricity estimator [129] from the instantaneous frequency of the GW using a Newtonian model. We assume that the GW frequency is twice the orbital frequency of a Newtonian orbit, but fit for additional degrees of freedom to model GR effects such as inspiral and precession of the orbit.

We estimate the eccentricity by fitting a short portion of the instantaneous GW frequency, ω_{GW} , to the form

$$\omega_{\text{GW}} = 2n(t) \frac{\sqrt{1-e^2}}{[1 - e \cos(u(t))]^2} \quad (16)$$

$$n(t) = n_0 [1 + a(t - t_{\text{ref}})] \quad (17)$$

$$u(t) = 2\pi(t - t_0)/P \quad (18)$$

in a neighbourhood of a reference time t_{ref} . This form for ω_{GW} is twice the orbital angular frequency expected from a Newtonian eccentric orbit, with the slow inspiral modeled as a linear variation of the parameter n with time. t_0 is a fitted parameter representing the time of pericentre passage, and a local maximum in ω_{GW} . We do not enforce the Newtonian relation $n = 2\pi/P$, since it is broken in the GR case by pericentre advance. $u(t)$ would properly be obtained using the Kepler equation. However, we do not find this necessary, and have effectively expanded it in small e . This expansion leads to good fits for the small values of e that we are simulating. It is necessary to include the nonlinear terms in e for the large-scale behavior of ω_{GW} in order to get a good fit when $e \gtrsim 0.1$. We find that using the coordinates of the horizon centroids, instead of the GW frequency, leads to qualitative disagreement with this simple Newtonian model, whereas the GW frequency matches very well.

Unlike the spin magnitudes and mass ratio, the eccentricity evolves significantly in the 14 orbits covered by the eccentric simulations, so assigning a single number to each configuration requires selecting a specific point in the evolution at which to quote the eccentricity.

We quote the eccentricity at a reference time t_{ref} at which the mean GW frequency $2n$ is 23.8 Hz assuming the source mass is $74 M_\odot$. This is $2Mn = 0.0545424$ in geometric units.

We obtain eccentricities up to $e = 0.13$ at the reference time; see Table II. Even “circular” NR waveforms have a small eccentricity, as it is not possible to reduce this to zero. For example, the smallest eccentricity in the family of waveforms considered here is $\sim 10^{-4}$, not 0.

We inject the above eccentric aligned-spin NR waveforms into zero noise and recover with the quasi-circular non-precessing EOBNR templates. Fig. 7 shows posteriors for the chirp mass, mass-ratio and aligned spin on the larger BH as a function of eccentricity. We find that eccentricities smaller than ~ 0.05 in the injected NR waveform (with the eccentricity definition introduced above) do not strongly affect parameter recovery and lead to results comparable to quasi-circular NR waveforms. Biases occur for larger eccentricity. The right

panel of Fig. 7 shows how the log likelihood drops sharply if the eccentricity is above 0.05 and the disagreement between the eccentric signal and quasi-circular template increases.

E. Effect of detector noise

So far in this study we have focussed on NR injections in zero noise using only an estimated PSD from the detectors in order to assess waveform systematics. The results obtained with this method are missing two potentially important effects:

- While we obtain the posterior probability density function effectively averaged over many noise realizations, the zero-noise method does not assess how noise realizations with typical deviations from the average will affect the posteriors.
- The usual interpretation of our credible intervals relies on the assumption that both our signal and noise model are an appropriate description of the data. The previous sections addressed the signal model, but the zero-noise method does not take into account the properties of actual detector noise, such as non-Gaussianity, non-stationarity and inaccuracies in PSD estimations.

In this section we study the variability of the posteriors for a selected NR waveform `SXS:BBH:0308` for several noise realizations. We compare with those examples the total uncertainty of PE (including noise realization) to the systematic error due to waveform model uncertainty from the previous sections.

We use LIGO-Hanford and LIGO-Livingston data from Monday September 14, 2015, surrounding GW150914. This data is produced using an updated calibration model, as described in [130, 131], which gives smaller uncertainties than the original 10% in amplitude and 10° in phase [103] used for the first results [1, 2]. For GW150914, the standard deviations of the prior distributions for the amplitude and phase uncertainty due to calibration are (as in Table III of [4]): amplitude Hanford: 4.8%, Livingston: 8.2% and phase Hanford: 3.2° , Livingston: 4.2° . The PE runs marginalize over calibration uncertainties with a spline model [2, 113].

We expect that for 90% of the noise realizations the 90% credible interval contains the injected value for a given quantity when both our model of the waveform and our noise-model (including the PSD) are correct. We see from Fig. 8 that most of the posteriors for the 13 different noise realizations agree reasonably, except for 11:07:48 where the posterior is bimodal in the chirp mass and thus very different from the zero-noise posterior. Results are broadly consistent between the EOBNR and IMRPhenom waveform models, and we find no evidence that the assumptions motivating our zero-noise study are violated.

F. Effect of numerical errors

NR simulations of black hole binaries can only be carried out with finite numerical resolution, which gives rise to truncation errors. SpEC uses *hp* adaptive mesh refinement to ensure accuracy and efficiency [80]. Each numerical resolution is indexed by $\text{Lev} = 0, \dots, n$. The truncation error is estimated at every step during the evolution, and the number of basis functions (or, equivalently, collocation points) is adjusted to ensure that the truncation error in all subdomains is less than a desired threshold (see e.g. [80] for more details).

Another possible source of error is in the extraction of the gravitational waveform itself. In SpEC, GWs are computed using the standard Regge-Wheeler-Zerilli (RWZ) formalism [132–134]. The waveforms are extracted on a sequence of concentric coordinate spherical shells centered on the origin of the grid [135]. To mitigate gauge and finite radius effects, the gravitational waveforms are then extrapolated to null infinity by performing polynomial fitting in powers of $1/r$ [88]. We label the polynomial degree of the fit by $N = 2, 3, 4$.

To assess the overall error, we choose a representative configuration `SXS:BBH:0308` consistent with GW150914 at fiducial orientation (see Table II) and compare the posteriors for different numerical grid resolutions and extrapolation orders.

In Fig. 9 we show kernel density estimates of 90% credible regions for posteriors from PE simulations on this NR waveform in zero noise varying the resolution and the extrapolation order. We find that the results for this NR waveform with different resolutions and extrapolation orders agree extremely well.

We expect these results to be typical for all of the NR waveforms that we have used. The mismatch error of the BAM waveforms (see Table II) is comparable to that of the representative SXS configuration `SXS:BBH:0308`, which suggests that parameter biases due to numerical error will also be negligible. We therefore conclude that our results are robust and the numerical error is not the dominant error source.

IV. DISCUSSION

The parameters of the source of the first GW observation, GW150914, were analyzed using waveform models from non-precessing [5, 6] and precessing [7, 9, 10] BBH coalescences. Both waveform models were calibrated to NR simulations, and are expected to be reliable for binary configurations similar to GW150914, i.e., black holes with comparable masses and low spins. The three models gave consistent results [2–4]. Nonetheless, there are several possible sources of systematic errors: the precessing IMRPhenom and EOBNR models were calibrated only to non-precessing NR simulations [8–10, 14]. In the case of the IMRPhenom model, the precession effects are described with approximate PN expressions; the six-dimensional spin-parameter space is described using only three judiciously chosen parameters, which were motivated by the dominant aligned and precession spin effects during the inspiral; and both models include only partial information about the sub-dominant harmonic modes of the signal.

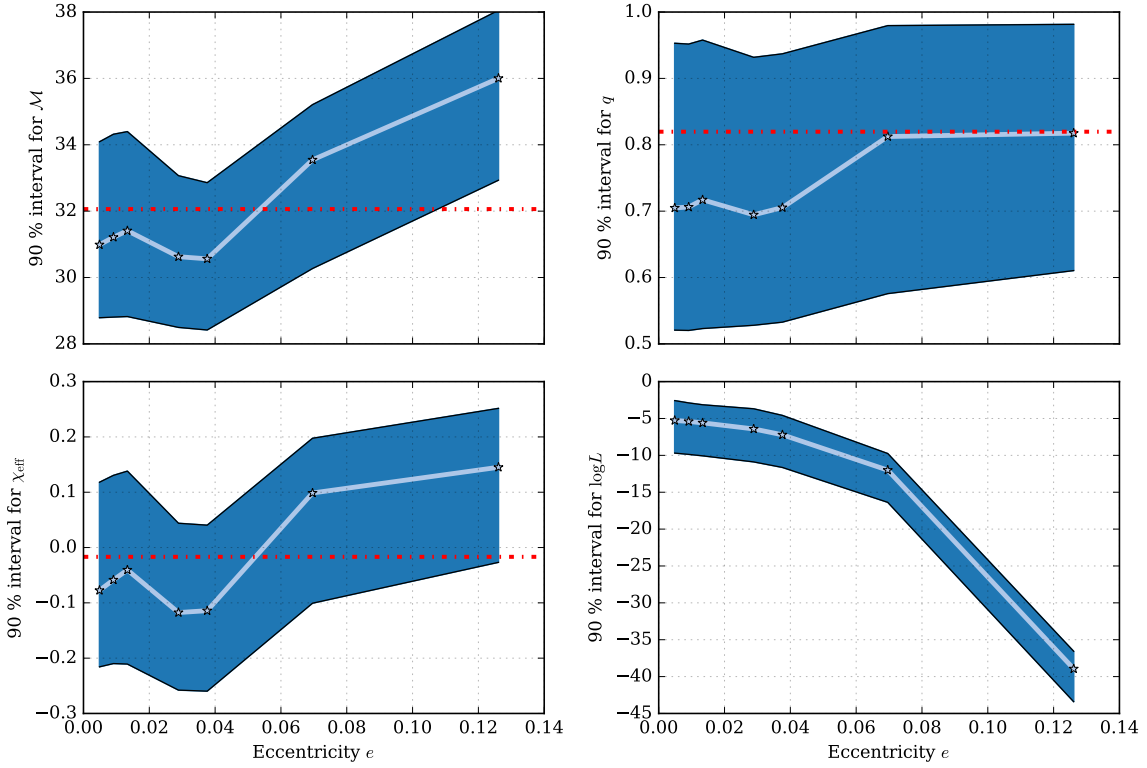


FIG. 7. Parameter recovery of eccentric NR mock signals with non-eccentric (quasi-circular) waveform templates. Shown are 90% credible intervals of non-precessing EOBNR posteriors for NR signals consistent with GW150914 injected in zero-noise. Shown is the chirp mass, mass-ratio, effective aligned spin and log-likelihood. As the eccentricity of the mock signals increases the deviation of the median of the chirp mass from the injected value grows. There is no significant disagreement in the mass-ratio and aligned spin. The likelihood drops sharply as the eccentricity grows beyond ~ 0.05 .

The present study expands on a brief analysis of parameter biases reported in Refs. [1–3] which indicated that the various waveform model deficiencies do not significantly impact PE for GW150914. Here, we use waveforms obtained by direct numerical solutions of the full Einstein equations, and inject these as mock signals into simulated aLIGO detector noise. Because of the high quality of numerical solutions of Einstein’s equations (cf. Fig. 9), the numerical waveforms can be taken as the prediction of Einstein’s equations, with negligible deviations from the exact GR waveforms. We then perform PE studies with the waveform models employed in [2] and carefully document any deviation of the recovered parameters from the parameters of the numerically simulated BBH systems.

The present study focuses specifically on BBH parameters comparable to those of GW150914. This is a fairly high-mass, nearly equal mass BBH system, with nearly vanishing effective spin parallel to the orbital angular momentum, χ_{eff} . The spin-magnitudes and spin-directions are not significantly constrained, except for the measurement of χ_{eff} .

The first study reported here concerns aligned-spin BBH systems, which do not precess. Recovering the parameters of such an injection with non-precessing EOBNR and IMR-Phenom waveform models yields unbiased recovered parameters, where the uncertainty in the recovered parameters is

dominated by statistical errors, without noticeable systematic biases (cf. Fig. 1). This result is consistent with extensive previous studies of aligned-spin waveform models, e.g. [43, 46, 114].

Focusing on the less-studied case of precessing binaries, Figs. 2 and 3 demonstrate that a precessing NR waveform near fiducial parameters consistent with GW150914 is recovered very well. The parameters of the injected NR waveform are near the centers of the recovered 90% credible intervals in the noise-free case, demonstrating confidently that any biases in the waveform models are small. For the spin-recovery, χ_{eff} is measured comparably well as in the GW150914 PE studies [2, 3]; the precession effects encoded in χ_p are not meaningfully constrained, again consistent with [2, 3]. The most likely parameters of GW150914 suggest that the binary’s inclination is nearly face-off, a configuration for which precession-induced modulations of the waveforms are small. Fig. 4 presents a study of different angles θ_{JN} between the total angular momentum and the line-of-sight, based on two numerical waveforms with different magnitude of precession spins χ_p . For most values of θ_{JN} , the injected parameters are recovered very well with no apparent systematic bias. However, if the system is viewed edge-on ($\theta_{\text{JN}} \approx 90^\circ$) and if the GW polarization happens to be unfavorable, biases can arise. For these particular cases, the waveform amplitudes are sig-

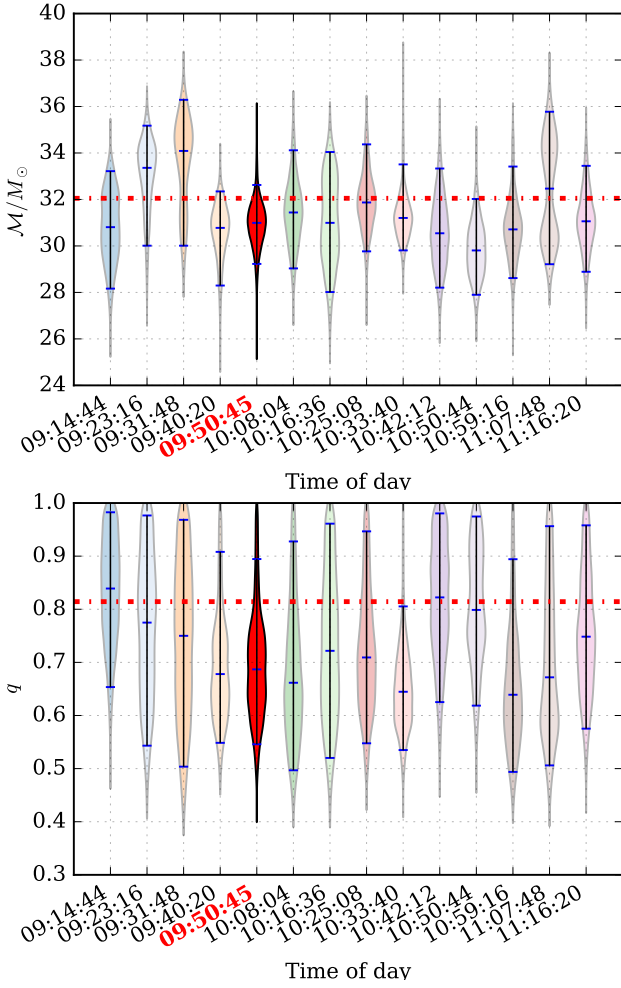


FIG. 8. Violin plots of the posteriors for an NR waveform (SXS:BBH:0308) injected into 13 different noise realizations on Monday September 14, 2015 (times in GMT) in the LIGO-Hanford and LIGO-Livingston data surrounding GW150914. The signal uses the fiducial values for the inclination and polarization angles. The PE runs used the non-precessing EOBNR as a template and spline calibration marginalization. The violins extend over the entire range of the PDF with medians and 90% credible intervals indicated by lines. The injected values of the parameters are marked by a red dash-dotted line. We show a violin for parameter recovery in zero-noise in red, labeled with the time of GW150914.

nificantly diminished because the detector orientation is near a node of *both* waveform polarizations¹², cf. Fig. 5. In these cases, the waveforms can significantly differ from the shapes of the model signal. Because only the dominant harmonic effects are included in the precessing IMRPhenom waveform model, and the precession effects through merger are captured only approximately, it is not surprising that parameter recovery is biased in this regime. As outlined in Appendix B, only

¹² The injections of Fig. 4 are performed at fixed signal-to-noise ratio, and so the diminished GW amplitude manifests itself in a smaller injected distance, cf. lowest panels of Fig. 4.

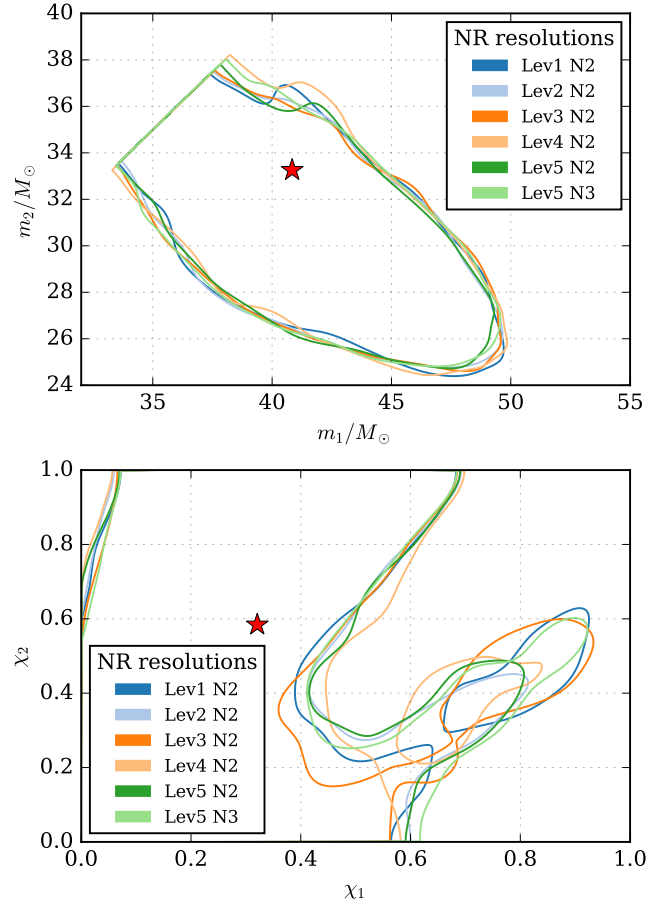


FIG. 9. 90% credible regions for configuration SXS:BBH:0308 with numerical resolutions $\text{Lev} = \{1, 2, 3, 4, 5\}$ and extrapolation orders $N = \{2, 3\}$. We find consistent results between the different resolutions and extrapolation orders, indicating that numerical errors are a negligible source of parameter biases.

a small fraction $\sim 0.3\%$ of BBH binaries detectable by aLIGO in the vicinity of GW150914 will fall into this biased edge-on regime.

Conversely, given the wide posteriors of GW150914, there is a small chance that the system's parameters are significantly different from the most likely values, and indeed, the source of GW150914 could be oriented edge-on. However, the posterior probability for strongly precessing systems oriented in this way is so small, that the waveform inaccuracies indicated by the study performed here (see Sec. III B 2 and Appendix B) should not significantly affect the 90% credible levels reported in the analysis of GW150914 [2].

The studies presented in Figs. 1 to 4 always inject the complete NR waveform (using all available numerical (ℓ, m) modes), whereas the recovery was performed with waveform models that model correctly only the $(2, \pm 2)$ modes. Therefore, the lack of bias in Figs. 1 to 4 already indicates that for GW150914-like signals, modeling of sub-dominant waveform modes is not necessary. This is confirmed by the study reported in Fig. 6.

All waveform models used to analyze GW150914 assume

circular orbits. Vanishingly small eccentricity is expected for field binaries [107, 136], and with the GW observations, this assumption can now be confronted with data. A measurement of eccentricity requires eccentric IMR waveform models, which are currently not available. But see [137]. However, we can inject eccentric mock NR waveforms, and quantify PE biases. This study is reported in Fig. 7: Eccentricities up to a few percent (measured at a GW frequency of 25 Hz) do not result in systematic PE biases, and only marginally reduce the likelihood. However, for $e > 0.05$, the likelihood drops significantly and parameter biases become appreciable.

Finally, we investigate the variations in PE estimates for different noise realizations. Injecting the identical NR signal into the aLIGO detector data at 13 different times around the time of GW150914, we find no evidence that our zero-noise injection study is based on false assumptions.

Overall, our analysis finds no significant bias of the original analysis of GW150914 [2]. GW150914 lies in a region of parameter space for which non-precessing binaries have received detailed study [5, 8, 43, 46, 114] and reliable waveform models exist. The parameter estimation results in Refs. [2, 3] and in the present paper suggest that either GW150914 did not include significant precession, or that precession effects did not leave a strong imprint on the signal. This is consistent with the high mass of the source, which causes only a few waveform cycles to be in aLIGO’s frequency band, and the comparable masses of the two black holes. In such systems we expect that precession effects are difficult to unambiguously distinguish unless the binary has a large inclination with respect to the observer.

In the vicinity of GW150914 we would expect biases if the source had significantly higher SNR than 25. In the high SNR regime the statistical errors decrease linearly with the inverse of the SNR. For the results shown in Figs. 1 to 4 parameters would therefore start to become biased at SNRs above $\sim 70 - 100$.

GW150914 lies in a region of parameter space which is fairly easy to model: The small number of observable GW cycles combined with a mass-ratio close to unity and modest spin magnitudes make this system easy to study with numerical relativity. Indeed simulations covering this part of BBH parameter space have been available for several years (e.g. [43, 138]) and are incorporated in current waveform models. Moreover, several properties of GW150914 suppress the importance of sub-dominant waveform modes and the importance of precession: Comparable mass, moderate spins, short duration, near face-on orientation. Waveform models are less mature for lower-mass systems, higher mass ratios, and larger spin magnitudes, and in these systems precession-induced waveform modulations may be easier to discern in the data. Therefore, we recommend that this study is repeated for BBH GW observations in other regions of parameter space.

ACKNOWLEDGMENTS

The authors gratefully acknowledge the support of the United States National Science Foundation (NSF) for the con-

struction and operation of the LIGO Laboratory and Advanced LIGO as well as the Science and Technology Facilities Council (STFC) of the United Kingdom, the Max-Planck-Society (MPS), and the State of Niedersachsen/Germany for support of the construction of Advanced LIGO and construction and operation of the GEO600 detector. Additional support for Advanced LIGO was provided by the Australian Research Council. The authors gratefully acknowledge the Italian Istituto Nazionale di Fisica Nucleare (INFN), the French Centre National de la Recherche Scientifique (CNRS) and the Foundation for Fundamental Research on Matter supported by the Netherlands Organisation for Scientific Research, for the construction and operation of the Virgo detector and the creation and support of the EGO consortium. The authors also gratefully acknowledge research support from these agencies as well as by the Council of Scientific and Industrial Research of India, Department of Science and Technology, India, Science & Engineering Research Board (SERB), India, Ministry of Human Resource Development, India, the Spanish Ministerio de Economía y Competitividad, the Conselleria d’Economia i Competitivitat and Conselleria d’Educació, Cultura i Universitats of the Govern de les Illes Balears, the National Science Centre of Poland, the European Commission, the Royal Society, the Scottish Funding Council, the Scottish Universities Physics Alliance, the Hungarian Scientific Research Fund (OTKA), the Lyon Institute of Origins (LIO), the National Research Foundation of Korea, Industry Canada and the Province of Ontario through the Ministry of Economic Development and Innovation, the Natural Science and Engineering Research Council Canada, Canadian Institute for Advanced Research, the Brazilian Ministry of Science, Technology, and Innovation, Fundação de Amparo à Pesquisa do Estado de São Paulo (FAPESP), Russian Foundation for Basic Research, the Leverhulme Trust, the Research Corporation, Ministry of Science and Technology (MOST), Taiwan and the Kavli Foundation. The authors gratefully acknowledge the support of the NSF, STFC, MPS, INFN, CNRS and the State of Niedersachsen/Germany for provision of computational resources.

CFUIB simulations were carried out on the UK DiRAC Datacentric cluster. The SXS simulations were carried out on HPC resources provided by Compute Canada, the Research Corporation, and California State University Fullerton, on the San Diego Supercomputer Center’s machine Comet and on the AEI Datura cluster. We further acknowledge support from the Research Corporation for Science Advancement, and the Sherman Fairchild Foundation.

Appendix A: Parameter estimation results for additional NR configurations

In addition to the NR runs presented in Table II, we have also analyzed a set of supplementary aligned-spin and precessing binary configurations as listed in Table III. Tables IV and V list the PE results for these additional configurations.

The aligned-spin cases, which span a range of mass ratios and spin magnitudes, were injected at the fiducial inclination angle of $\iota = 163^\circ$ and analyzed with the non-precessing

EOBNR [5, 6] and IMRPhenom [8] waveform models. The NR signal includes all higher modes. Differences to results for injections with just the $\ell = |m| = 2$ modes are very small. Overall, we find highly consistent results between the two waveform families. This is particularly true for the equal-mass cases, where both models recover the effective spin (see Eq. (3)) and the chirp mass accurately, with the most biased physical parameter being the mass ratio. Although, for decreased mass ratios we find that the recovery of q improves. We note, however, that for the equal mass case the mass ratio lies on the boundary of the physically allowed space, so the median estimate must always be biased. The effective aligned spin χ_{eff} is well recovered with biases smaller than 0.1 for all cases. In addition, we observe a weak correlation between the bias in the chirp mass and the bias in the effective spin. For SXS:BBH:0257 and SXS:BBH:0233 we find noticeable biases in the mass-ratio recovery of EOBNR. In addition, for SXS:BBH:0233 we find very broad PDFs in the chirp mass for both models, but more markedly for EOBNR. The posteriors obtained from the non-precessing EOBNR for SXS:BBH:0257 are bimodal in chirp-mass, mass-ratio and effective spin. This simulation was previously found to significantly disagree with EOBNR [46], having a mismatch of about 10%. While these configurations have high component spins and lie at the edge of the calibration ranges of EOBNR (both cases) and IMRPhenom (SXS:BBH:0233) where their accuracy may be diminished, we emphasize that for the configurations near the most likely parameters of GW150914 both models recover the NR parameters very accurately. We do not show results for the anti-symmetric combination of aligned spins since it is in general poorly constrained [118].

For the three additional precessing cases, which were analyzed only with the precessing IMRPhenom waveform model [7], we find qualitatively similar results, although we emphasize again that the small number of configurations does not allow to make global statements. Nevertheless, out of the three cases we find that the mass ratio is determined best for the $q = 0.333$ run. Similar to the aligned-spin runs, we find that large biases in χ_{eff} are correlated with large biases in the chirp mass. For all except one configuration, we find that the precession spin χ_p is underestimated, with only minimal improvement when the inclination angle is changed from nearly face-off to edge-on inclination. χ_{eff} on the other hand is very well determined with a bias smaller than 0.1. Only for edge-on inclination and the fiducial polarization value can the bias become large.

Appendix B: Distribution of detectable polarization and inclination

Here we provide a simple, but instructive estimate of how many observations are expected to fall into a given range of orientations (i.e., have particular polarization and inclination angles). This question arose in Sec. III B 2 where the signals with largest bias were found to be characterized by a specific orientation. Our analysis follows because the binary, with so little time to precess in band, can be reasonably approximated

by a non-precessing binary for the time interval of greatest interest.

We start from the detector response, cf. Eq. (9), and the antenna response functions $F_{+,\times}$ that depend on the polarization-angle ψ and sky-location. In an Earth-centered coordinate system, the position of the GW source on the celestial sphere is given by the spherical polar coordinates (β, ϕ) , where β is related to the declination δ and ϕ to the right ascension α (see [95] for details). The antenna response functions then read as

$$\begin{aligned} F_+ &= -\frac{1 + \cos^2 \beta}{2} \cos 2\phi \cos 2\psi - \cos \beta \sin 2\phi \sin 2\psi, \\ F_\times &= \frac{1 + \cos^2 \beta}{2} \cos 2\phi \sin 2\psi - \cos \beta \sin 2\phi \cos 2\psi. \end{aligned} \quad (\text{B1})$$

Trigonometric identities allow us to recast (B1) into the following form

$$\begin{aligned} F_+ &= -A_{\text{sky}} \cos(2\psi - \Xi), \\ F_\times &= A_{\text{sky}} \sin(2\psi - \Xi), \end{aligned} \quad (\text{B2})$$

where

$$\begin{aligned} A_{\text{sky}} &= \sqrt{\frac{(1 + \cos^2 \beta)^2}{4} \cos^2 2\phi + \cos^2 \beta \sin^2 2\phi}, \\ \Xi &= \arctan\left(\frac{2 \cos \beta}{1 + \cos^2 \beta} \tan 2\phi\right). \end{aligned} \quad (\text{B3})$$

For non-precessing binaries and to lowest PN order, the source inclination, ι , enters the amplitude of the GW polarizations $h_{+,\times}$ in the following way [139],

$$\begin{aligned} h_+ &= (1 + \cos^2 \iota) A_{\text{GW}} \cos(\phi_{\text{GW}}), \\ h_\times &= -2 \cos \iota A_{\text{GW}} \sin(\phi_{\text{GW}}). \end{aligned} \quad (\text{B5})$$

Using (B2) and (B5), we can now recast the detector response Eq. (9) as

$$h_{\text{resp}} = A_{\text{GW}} A_{\text{sky}} A_{\text{pol}} \cos(\Phi_{\text{GW}} - \Phi_0). \quad (\text{B6})$$

Here, A_{GW} depends on the binary's masses, spins and time; A_{sky} depends solely on the sky location, and A_{pol} describes the amplitude variation with inclination and polarization,

$$A_{\text{pol}} = \sqrt{(1 + \cos^2 \iota)^2 \cos^2(2\psi - \Xi) + 4 \cos^2 \iota \sin^2(2\psi - \Xi)}. \quad (\text{B7})$$

Φ_0 is a simple shift in the phase of h ,

$$\Phi_0 = \pi + \arctan\left[\frac{2 \cos \iota}{1 + \cos^2 \iota} \tan(2\psi - \Xi)\right]. \quad (\text{B8})$$

We now assume that signals with an SNR above an arbitrary threshold are detectable. The SNR is proportional to the signal amplitude which in turn scales linearly with the inverse of the distance between source and detector. Assuming uniformly distributed sources, the number of detectable signals is proportional to the cubed distance, hence we can integrate A_{pol}^3 [all other amplitude terms in (B2) are constant] over polarization, ψ , and inclination, $\cos \iota$ (using isotropic priors), to

ID	q	χ_1	χ_2	χ_{eff}	χ_p	$M\Omega$	N_{orbits}	e	$1 - \mathcal{O}_{\text{res}}$
SXS:BBH:0211	1.0	(0.0,0.0,-0.8997)	(0.0,0.0,0.8998)	0.0	0.0	0.014107	22.3	0.00026	4.1×10^{-4}
SXS:BBH:0213	1.0	(0.0,0.0,-0.7998)	(0.0,0.0,0.7999)	0.0	0.0	0.014346	22.3	0.00014	5.2×10^{-4}
SXS:BBH:0180	1.0	(0.0,0.0,0.0)	(0.0,0.0,0.0)	0.0	0.0	0.01227	28.2	0.00005	5.5×10^{-4}
SXS:BBH:0219	1.0	(0.0,0.0,-0.5)	(0.0,0.0,0.8998)	0.2	0.0	0.014836	22.4	0.00033	2.5×10^{-4}
SXS:BBH:0229	1.0	(0.0,0.0,0.65)	(0.0,0.0,0.25)	0.45	0.0	0.014879	23.1	0.00031	1.8×10^{-4}
SXS:BBH:0231	1.0	(0.0,0.0,0.8998)	(0.0,0.0,0.0)	0.4499	0.0	0.014874	23.1	$< 1 \times 10^{-4}$	2.4×10^{-4}
SXS:BBH:0152	1.0	(0.0,0.0,0.6)	(0.0,0.0,0.6)	0.6	0.0	0.015529	22.6	0.00043	3×10^{-5}
SXS:BBH:0214	1.0	(0.0,0.0,-0.6249)	(0.0,0.0,-0.25)	-0.4375	0.0	0.012637	24.4	0.00019	1.1×10^{-4}
SXS:BBH:0311	0.84	(0.0,0.4199)	(0.0,0.3800)	0.4017	0.0	0.017507	18.2	1.2×10^{-4}	2.9×10^{-4}
SXS:BBH:0310	0.82	(0.0,0)	(0.0,0)	0.0	0.0	0.018230	15.2	7.7×10^{-4}	4.1×10^{-5}
SXS:BBH:0309	0.82	(0.0, 0.0, 0.3302)	(0.0, 0.0, -0.4398)	-0.0165	0.0	0.017942	15.7	0.02763	5.4×10^{-4}
SXS:BBH:0305	0.82	(0.0,0.3301)	(0.0,-0.4399)	-0.0166	0.0	0.018208	15.2	2.5×10^{-4}	3×10^{-4}
SXS:BBH:0019	0.667	(0.0,0.0,-0.4995)	(0.0,0.0,0.4995)	-0.0999	0.0	0.014604	20.4	$< 7.6 \times 10^{-5}$	5.5×10^{-4}
SXS:BBH:0239	0.5	(0.0,0.0,-0.3713)	(0.0,0.0,0.8497)	0.0358	0.0	0.014782	22.2	$< 9.1 \times 10^{-5}$	2.2×10^{-5}
SXS:BBH:0257	0.5	(0.0,0.0,0.8498)	(0.0,0.0,0.8498)	0.8498	0.0	0.016332	24.8	0.00011	3×10^{-4}
SXS:BBH:0233	0.5	(0.0,0.0,-0.8713)	(0.0,0.0,0.8497)	-0.2976	0.0	0.014232	22.0	0.00006	3.2×10^{-4}
SXS:BBH:0065	0.125	(0.0,0.0,0.4996)	(0.0,0.0,0.0)	0.4441	0.0	0.018869	34.0	0.00374	7.8×10^{-4}
SXS:BBH:0522	0.588	(0.0787,0.5729,-0.5527)	(-0.0509,0.033,-0.7974)	-0.655	0.5588	0.015463	16.7	0.0002321	9.4×10^{-4}
SXS:BBH:0531	0.588	(-0.2992,0.4469,0.5925)	(0.0787,0.0269,0.7954)	0.6601	0.5509	0.017381	21.4	$< 1.5 \times 10^{-4}$	2.8×10^{-4}
SXS:BBH:0049	0.333	(0.4941,0.0733,0.0011)	(-0.0002,-0.008,0.4993)	0.1267	0.4995	0.017518	19.4	0.00041	n/a

TABLE III. Parameters of additional NR runs from the public SXS waveform catalog [13, 85], the non-public catalog [86] and new simulations targeted at GW150914 [87]. The columns are as defined in Table II.

estimate how many observations would fall into a particular range of source orientations.

We find that there is only a 0.3% chance of a detectable signal to fall into a $30^\circ \times 30^\circ$ region in inclination and polarization around the point of minimal amplitude (which we take approximately as the point of maximal bias).

We stress that this estimate relies on leading order expansions of the amplitude and assumes a fixed region in inclination-polarization space, independently of the SNR. We can drop the first assumption by repeating the calculation with

precessing NR waveforms, and we find comparable results. However, whether or not sources show biased parameter estimates (the original question posed in Sec. III B 2) depends of course not only on the orientation, but on the intrinsic parameters and the SNR of the source; exploring these parameter dependencies is a long-term goal requiring many more simulation and analysis campaigns. What we have presented here is an illustration with basic calculations that only a small fraction of observable sources is expected to be in the most problematic region of orientations.

- [1] B. P. Abbott *et al.* (Virgo, LIGO Scientific), *Phys. Rev. Lett.* **116**, 061102 (2016), arXiv:1602.03837 [gr-qc].
- [2] B. P. Abbott *et al.* (Virgo, LIGO Scientific), *Phys. Rev. Lett.* **116**, 241102 (2016), arXiv:1602.03840 [gr-qc].
- [3] B. Abbott *et al.* (Virgo, LIGO Scientific), *Phys. Rev.* **X6**, 041014 (2016), arXiv:1606.01210 [gr-qc].
- [4] B. P. Abbott *et al.* (Virgo, LIGO Scientific), *Phys. Rev.* **X6**, 041015 (2016), arXiv:1606.04856 [gr-qc].
- [5] A. Taracchini, A. Buonanno, Y. Pan, T. Hinderer, M. Boyle, *et al.*, *Phys. Rev.* **D89**, 061502 (2014), arXiv:1311.2544 [gr-qc].
- [6] M. Pürrer, *Phys. Rev.* **D93**, 064041 (2016), arXiv:1512.02248 [gr-qc].
- [7] M. Hannam, P. Schmidt, A. Bohé, L. Haegel, S. Husa, F. Ohme, G. Pratten, and M. Pürrer, *Phys. Rev. Lett.* **113**, 151101 (2014), arXiv:1308.3271 [gr-qc].
- [8] S. Khan, S. Husa, M. Hannam, F. Ohme, M. Pürrer, X. Jiménez Forteza, and A. Bohé, *Phys. Rev.* **D93**, 044007 (2016), arXiv:1508.07253 [gr-qc].
- [9] Y. Pan, A. Buonanno, A. Taracchini, L. E. Kidder, A. H. Mroué, H. P. Pfeiffer, M. A. Scheel, and B. Szilágyi, *Phys. Rev.* **D89**, 084006 (2014), arXiv:1307.6232 [gr-qc].
- [10] S. Babak, A. Taracchini, and A. Buonanno, *Phys. Rev.* **D95**, 024010 (2017), arXiv:1607.05661 [gr-qc].
- [11] M. Alcubierre, *Introduction to 3+1 Numerical Relativity* (Oxford University Press, 2008).
- [12] T. W. Baumgarte and S. L. Shapiro, *Numerical Relativity. Solving Einstein's Equations on the Computer* (Cambridge University Press, 2010).
- [13] A. H. Mroué *et al.*, *Phys. Rev. Lett.* **111**, 241104 (2013), arXiv:1304.6077 [gr-qc].
- [14] S. Husa, S. Khan, M. Hannam, M. Pürrer, F. Ohme, X. Jiménez Forteza, and A. Bohé, *Phys. Rev.* **D93**, 044006 (2016), arXiv:1508.07250 [gr-qc].
- [15] L. Blanchet, *Living Rev. Rel.* **17**, 2 (2014), arXiv:1310.1528 [gr-qc].
- [16] T. A. Apostolatos, C. Cutler, G. J. Sussman, and K. S. Thorne, *Phys. Rev. D* **49**, 6274 (1994).
- [17] L. E. Kidder, *Phys. Rev.* **D52**, 821 (1995), arXiv:gr-qc/9506022 [gr-qc].
- [18] P. Schmidt, F. Ohme, and M. Hannam, *Phys. Rev.* **D91**, 024043 (2015), arXiv:1408.1810 [gr-qc].

	\mathcal{M}				q				χ_{eff}			
	True	Median	Bias	90% CI	True	Median	Bias	90% CI	True	Median	Bias	90% CI
SXS:BBH:0211												
EOBNR	32.25	31.22	1.03	5.15	1.00	0.71	0.29	0.42	0.00	-0.06	0.06	0.33
IMRPhenom	32.25	31.81	0.44	4.23	1.00	0.82	0.18	0.38	0.00	-0.02	0.02	0.24
SXS:BBH:0213												
EOBNR	32.25	31.04	1.21	5.70	1.00	0.68	0.32	0.44	0.00	-0.07	0.07	0.35
IMRPhenom	32.25	32.16	0.09	4.28	1.00	0.81	0.19	0.40	0.00	0.00	-0.00	0.24
SXS:BBH:0180												
EOBNR	32.25	31.20	1.06	5.34	1.00	0.71	0.29	0.43	-0.00	-0.07	0.07	0.33
IMRPhenom	32.25	31.88	0.38	4.16	1.00	0.82	0.18	0.38	-0.00	-0.02	0.02	0.24
SXS:BBH:0219												
EOBNR	32.25	32.67	-0.41	3.29	1.00	0.80	0.20	0.40	0.20	0.21	-0.01	0.21
IMRPhenom	32.25	32.16	0.10	3.60	1.00	0.79	0.21	0.40	0.20	0.20	0.00	0.21
SXS:BBH:0229												
EOBNR	32.25	32.41	-0.16	3.94	1.00	0.80	0.20	0.43	0.45	0.43	0.02	0.27
IMRPhenom	32.25	31.92	0.33	2.94	1.00	0.79	0.21	0.42	0.45	0.43	0.02	0.17
SXS:BBH:0231												
EOBNR	32.25	32.48	-0.23	3.95	1.00	0.80	0.20	0.43	0.45	0.43	0.02	0.28
IMRPhenom	32.25	31.97	0.28	3.00	1.00	0.79	0.21	0.44	0.45	0.43	0.02	0.18
SXS:BBH:0152												
EOBNR	32.25	32.85	-0.59	3.63	1.00	0.81	0.19	0.44	0.60	0.62	-0.02	0.30
IMRPhenom	32.25	31.79	0.46	2.66	1.00	0.79	0.21	0.43	0.60	0.57	0.03	0.16
SXS:BBH:0214												
EOBNR	32.25	30.66	1.59	4.99	1.00	0.78	0.22	0.40	-0.44	-0.52	0.08	0.30
IMRPhenom	32.25	31.64	0.61	4.92	1.00	0.80	0.20	0.41	-0.44	-0.46	0.02	0.29
SXS:BBH:0311												
EOBNR	32.11	32.32	-0.21	3.47	0.84	0.79	0.05	0.44	0.40	0.38	0.02	0.23
IMRPhenom	32.11	31.91	0.20	3.14	0.84	0.78	0.06	0.44	0.40	0.39	0.02	0.19
SXS:BBH:0310												
EOBNR	32.06	31.43	0.63	5.54	0.82	0.71	0.11	0.44	0.00	-0.04	0.04	0.34
IMRPhenom	32.06	31.85	0.21	4.46	0.82	0.80	0.02	0.40	0.00	-0.02	0.02	0.25
SXS:BBH:0309												
EOBNR	32.06	31.22	0.85	5.27	0.82	0.73	0.09	0.43	-0.02	-0.05	0.04	0.34
IMRPhenom	32.06	31.70	0.36	4.11	0.82	0.81	0.00	0.38	-0.02	-0.02	0.01	0.24
SXS:BBH:0305												
EOBNR	32.06	31.27	0.79	5.48	0.82	0.72	0.10	0.43	-0.02	-0.06	0.04	0.34
IMRPhenom	32.06	31.79	0.27	4.16	0.82	0.81	0.01	0.40	-0.02	-0.02	0.01	0.24
SXS:BBH:0307												
EOBNR	32.05	31.32	0.73	4.59	0.81	0.73	0.09	0.40	-0.08	-0.12	0.04	0.31
IMRPhenom	32.05	31.58	0.47	4.12	0.81	0.83	-0.01	0.38	-0.08	-0.10	0.01	0.25
SXS:BBH:0019												
EOBNR	31.47	32.24	-0.77	6.19	0.67	0.69	-0.03	0.45	-0.10	-0.10	0.00	0.37
IMRPhenom	31.47	32.66	-1.19	5.40	0.67	0.75	-0.08	0.46	-0.10	-0.08	-0.02	0.27
SXS:BBH:0239												
EOBNR	30.05	31.31	-1.26	7.93	0.50	0.52	-0.02	0.50	0.04	0.02	0.02	0.40
IMRPhenom	30.05	29.96	0.09	6.70	0.50	0.46	0.04	0.35	0.04	-0.04	0.07	0.30
SXS:BBH:0257												
EOBNR	30.05	28.84	1.21	3.97	0.50	0.35	0.15	0.69	0.85	0.86	-0.01	0.18
IMRPhenom	30.05	29.96	0.09	2.17	0.50	0.51	-0.01	0.27	0.85	0.84	0.01	0.15
SXS:BBH:0233												
EOBNR	30.05	32.80	-2.75	12.00	0.50	0.64	-0.14	0.60	-0.30	-0.32	0.02	0.57
IMRPhenom	30.05	29.56	0.49	9.37	0.50	0.44	0.06	0.40	-0.30	-0.39	0.09	0.38
SXS:BBH:0065												
EOBNR	18.47	18.08	0.39	1.17	0.12	0.13	-0.00	0.05	0.44	0.39	0.05	0.11
IMRPhenom	18.47	18.51	-0.04	1.24	0.12	0.13	-0.00	0.04	0.44	0.46	-0.01	0.10

TABLE IV. True values, medians, absolute biases (difference between true value and the median) and the width of 90% credible intervals for several additional aligned-spin NR configurations (see Table II for the parameters of SXS:BBH:0307 and Table III for all other NR simulation parameters). The results are given for the chirp mass \mathcal{M} , the mass-ratio q , and the effective aligned spin χ_{eff} . The NR waveforms are injected at fiducial inclination angle $\iota = 163^\circ$, and parameter estimation is performed using the non-precessing EOBNR and the non-precessing IMRPhenom models.

	$\mathcal{M} (M_{\odot})$			q			χ_{eff}			χ_p		
	Median	Bias	90% CI	Median	Bias	90% CI	Median	Bias	90% CI	Median	Bias	90% CI
SXS:BBH:0049	$\mathcal{M} = 27.15 M_{\odot}$			$q = 0.3$			$\chi_{\text{eff}} = 0.13$			$\chi_p = 0.5$		
$\iota = 163^\circ$	27.47	-0.32	4.92	0.31	0.02	0.18	0.14	-0.01	0.24	0.20	0.30	0.46
$\iota = 90^\circ$	20.28	6.87	3.44	0.28	0.05	0.12	-0.66	0.78	0.28	0.14	0.36	0.13
$\iota = 90^\circ, \psi = 120^\circ$	29.06	-1.92	6.28	0.33	0.01	0.14	0.19	-0.06	0.33	0.60	-0.10	0.28
SXS:BBH:0522	$\mathcal{M} = 30.79 M_{\odot}$			$q = 0.57$			$\chi_{\text{eff}} = -0.65$			$\chi_p = 0.56$		
$\iota = 163^\circ$	32.63	-1.84	5.21	0.79	-0.22	0.42	-0.56	-0.09	0.30	0.39	0.17	0.50
$\iota = 90^\circ$	30.26	0.53	9.46	0.46	0.11	0.58	-0.55	-0.11	0.46	0.36	0.20	0.59
$\iota = 90^\circ, \psi = 120^\circ$	31.06	-0.27	5.98	0.67	-0.10	0.49	-0.63	-0.03	0.35	0.39	0.17	0.48
SXS:BBH:0531	$\mathcal{M} = 30.8 M_{\odot}$			$q = 0.57$			$\chi_{\text{eff}} = 0.66$			$\chi_p = 0.55$		
$\iota = 163^\circ$	30.29	0.51	3.08	0.46	0.11	0.35	0.61	0.05	0.19	0.36	0.19	0.45
$\iota = 90^\circ$	27.06	3.73	4.26	0.25	0.32	0.13	0.50	0.16	0.22	0.38	0.17	0.37
$\iota = 90^\circ, \psi = 120^\circ$	30.51	0.29	3.32	0.44	0.13	0.34	0.63	0.03	0.20	0.29	0.26	0.44

TABLE V. Medians, absolute biases (difference between injected value and the median) and the width of 90% credible intervals for several SXS configurations (see Table III). The results are given for the chirp mass \mathcal{M} , the mass-ratio q , the effective aligned spin χ_{eff} and the effective precession spin χ_p . The precessing IMRPhenom model was used as a template for the fiducial inclination and edge-on inclination $\iota = 90^\circ$. The polarization angle is fixed to the fiducial value $\psi \sim 82^\circ$, except where indicated.

- [19] A. Bohé, M. Hannam, S. Husa, F. Ohme, M. Pürrer, and P. Schmidt, In preparation (2016).
- [20] B. P. Abbott *et al.* (Virgo, LIGO Scientific), *Phys. Rev. Lett.* **116**, 241103 (2016), [arXiv:1606.04855 \[gr-qc\]](#).
- [21] T. A. Apostolatos, *Phys. Rev. D* **52**, 605 (1995).
- [22] P. Ajith, M. Hannam, S. Husa, Y. Chen, B. Brügmann, N. Dorband, D. Müller, F. Ohme, D. Pollney, C. Reisswig, L. Santamaría, and J. Seiler, *Phys. Rev. Lett.* **106**, 241101 (2011), [arXiv:0909.2867 \[gr-qc\]](#).
- [23] L. Santamaría, F. Ohme, P. Ajith, B. Brügmann, N. Dorband, *et al.*, *Phys. Rev.* **D82**, 064016 (2010), [arXiv:1005.3306 \[gr-qc\]](#).
- [24] B. P. Abbott *et al.* (Virgo, LIGO Scientific), *Phys. Rev.* **D94**, 064035 (2016), [arXiv:1606.01262 \[gr-qc\]](#).
- [25] K. Jani, J. Healy, J. A. Clark, L. London, P. Laguna, and D. Shoemaker, *Class. Quant. Grav.* **33**, 204001 (2016), [arXiv:1605.03204 \[gr-qc\]](#).
- [26] B. P. Abbott *et al.* (Virgo, LIGO Scientific), *Phys. Rev.* **D93**, 122004 (2016), [arXiv:1602.03843 \[gr-qc\]](#).
- [27] A. Buonanno and T. Damour, *Phys. Rev.* **D59**, 084006 (1999), [arXiv:gr-qc/9811091 \[gr-qc\]](#).
- [28] A. Buonanno and T. Damour, *Phys. Rev.* **D62**, 064015 (2000), [arXiv:gr-qc/0001013 \[gr-qc\]](#).
- [29] T. Damour and A. Nagar, *Phys. Rev.* **D76**, 064028 (2007), [arXiv:0705.2519 \[gr-qc\]](#).
- [30] T. Damour, B. R. Iyer, and A. Nagar, *Phys. Rev.* **D79**, 064004 (2009), [arXiv:0811.2069 \[gr-qc\]](#).
- [31] Y. Pan, A. Buonanno, R. Fujita, E. Racine, and H. Tagoshi, *Phys. Rev.* **D83**, 064003 (2011), [Erratum: *Phys. Rev. D* **87**, no. 10, 109901 (2013)], [arXiv:1006.0431 \[gr-qc\]](#).
- [32] E. Berti, V. Cardoso, and C. M. Will, *Phys. Rev.* **D73**, 064030 (2006), [arXiv:gr-qc/0512160](#).
- [33] L. London, D. Shoemaker, and J. Healy, *Phys. Rev.* **D90**, 124032 (2014), [arXiv:1404.3197 \[gr-qc\]](#).
- [34] T. Damour, A. Nagar, M. Hannam, S. Husa, and B. Brügmann, *Phys. Rev. D* **78**, 044039 (2008).
- [35] Y. Pan, A. Buonanno, M. Boyle, L. T. Buchman, L. E. Kidder, H. P. Pfeiffer, and M. A. Scheel, *Phys. Rev.* **D84**, 124052 (2011), [arXiv:1106.1021 \[gr-qc\]](#).
- [36] A. Taracchini, Y. Pan, A. Buonanno, E. Barausse, M. Boyle, T. Chu, G. Lovelace, H. P. Pfeiffer, and M. A. Scheel, *Phys. Rev.* **D86**, 024011 (2012), [arXiv:1202.0790 \[gr-qc\]](#).
- [37] T. Damour and A. Nagar, *Phys. Rev.* **D90**, 044018 (2014), [arXiv:1406.6913 \[gr-qc\]](#).
- [38] M. Boyle, A. Buonanno, L. E. Kidder, A. H. Mroué, Y. Pan, H. P. Pfeiffer and M. A. Scheel, *Phys. Rev. D* **78**, 104020 (2008), [arXiv:0804.4184 \[gr-qc\]](#).
- [39] G. Lovelace, M. Boyle, M. A. Scheel, and B. Szilagyi, *Class. Quant. Grav.* **29**, 045003 (2012), [arXiv:1110.2229 \[gr-qc\]](#).
- [40] T. Damour, A. Nagar, D. Pollney, and C. Reisswig, *Phys. Rev. Lett.* **108**, 131101 (2012), [arXiv:1110.2938 \[gr-qc\]](#).
- [41] L. T. Buchman, H. P. Pfeiffer, M. A. Scheel, and B. Szilagyi, *Phys. Rev.* **D86**, 084033 (2012), [arXiv:1206.3015 \[gr-qc\]](#).
- [42] A. Nagar, T. Damour, C. Reisswig, and D. Pollney, *Phys. Rev.* **D93**, 044046 (2016), [arXiv:1506.08457 \[gr-qc\]](#).
- [43] I. Hinder *et al.*, *Class. Quant. Grav.* **31**, 025012 (2014), [arXiv:1307.5307 \[gr-qc\]](#).
- [44] B. Szilágyi, J. Blackman, A. Buonanno, A. Taracchini, H. P. Pfeiffer, M. A. Scheel, T. Chu, L. E. Kidder, and Y. Pan, *Phys. Rev. Lett.* **115**, 031102 (2015), [arXiv:1502.04953 \[gr-qc\]](#).
- [45] P. Kumar, K. Barkett, S. Bhagwat, N. Afshari, D. A. Brown, G. Lovelace, M. A. Scheel, and B. Szilágyi, *Phys. Rev.* **D92**, 102001 (2015), [arXiv:1507.00103 \[gr-qc\]](#).
- [46] P. Kumar, T. Chu, H. Fong, H. P. Pfeiffer, M. Boyle, D. A. Hemberger, L. E. Kidder, M. A. Scheel, and B. Szilagyi, *Phys. Rev.* **D93**, 104050 (2016), [arXiv:1601.05396 \[gr-qc\]](#).
- [47] M. Pürrer, *Class. Quant. Grav.* **31**, 195010 (2014), [arXiv:1402.4146 \[gr-qc\]](#).
- [48] C. Devine, Z. B. Etienne, and S. T. McWilliams, *Class. Quant. Grav.* **33**, 125025 (2016), [arXiv:1601.03393 \[astro-ph.HE\]](#).
- [49] E. Barausse and A. Buonanno, *Phys. Rev.* **D81**, 084024 (2010), [arXiv:0912.3517 \[gr-qc\]](#).
- [50] E. Barausse and A. Buonanno, *Phys. Rev.* **D84**, 104027 (2011), [arXiv:1107.2904 \[gr-qc\]](#).
- [51] M. Boyle, R. Owen, and H. P. Pfeiffer, *Phys. Rev.* **D84**, 124011 (2011), [arXiv:1110.2965 \[gr-qc\]](#).
- [52] P. Ajith *et al.*, *Class. Quantum Grav.* **24**, S689 (2007), [arXiv:0704.3764](#).
- [53] Y. Pan, A. Buonanno, J. G. Baker, J. Centrella, B. J. Kelly, S. T. McWilliams, F. Pretorius, and J. R. van Meter, *Phys.*

- Rev. **D77**, 024014 (2008), arXiv:0704.1964 [gr-qc].
- [54] P. Schmidt, M. Hannam, S. Husa, and P. Ajith, *Phys. Rev. D* **84**, 024046 (2011), arXiv:1012.2879 [gr-qc].
- [55] P. Schmidt, M. Hannam, and S. Husa, *Phys. Rev. D* **86**, 104063 (2012), arXiv:1207.3088 [gr-qc].
- [56] E. E. Flanagan and S. A. Hughes, *Phys. Rev. D* **57**, 4566 (1998), arXiv:gr-qc/9710129 [gr-qc].
- [57] L. Lindblom, B. J. Owen, and D. A. Brown, *Phys. Rev. D* **78**, 124020 (2008), arXiv:0809.3844.
- [58] S. T. McWilliams, B. J. Kelly, and J. G. Baker, *Phys. Rev. D* **82**, 024014 (2010), arXiv:1004.0961 [gr-qc].
- [59] T. B. Littenberg, J. G. Baker, A. Buonanno, and B. J. Kelly, *Phys. Rev. D* **87**, 104003 (2013), arXiv:1210.0893 [gr-qc].
- [60] <http://www.black-holes.org/SpEC.html>.
- [61] M. A. Scheel, H. P. Pfeiffer, L. Lindblom, L. E. Kidder, O. Rinne, and S. A. Teukolsky, *Phys. Rev. D* **74**, 104006 (2006), arXiv:gr-qc/0607056 [gr-qc].
- [62] B. Szilágyi, L. Lindblom, and M. A. Scheel, *Phys. Rev. D* **80**, 124010 (2009), arXiv:0909.3557 [gr-qc].
- [63] B. Brügmann, J. A. González, M. Hannam, S. Husa, U. Sperhake, and W. Tichy, *Phys. Rev. D* **77**, 024027 (2008).
- [64] S. Husa, J. A. González, M. Hannam, B. Brügmann, and U. Sperhake, *Classical and Quantum Gravity* **25**, 105006 (2008).
- [65] M. Shibata and T. Nakamura, *Phys. Rev. D* **52**, 5428 (1995).
- [66] T. W. Baumgarte and S. L. Shapiro, *Phys. Rev. D* **59**, 024007 (1998).
- [67] M. Campanelli, C. O. Lousto, P. Marronetti, and Y. Zlochower, *Phys. Rev. Lett.* **96**, 111101 (2006), arXiv:gr-qc/0511048.
- [68] J. G. Baker, J. Centrella, D.-I. Choi, M. Koppitz, and J. van Meter, *Phys. Rev. Lett.* **96**, 111102 (2006), arXiv:gr-qc/0511103.
- [69] G. B. Cook and J. W. York, Jr., *Phys. Rev. D* **41**, 1077 (1990).
- [70] S. Brandt and B. Bruegmann, *Phys. Rev. Lett.* **78**, 3606 (1997), arXiv:gr-qc/9703066 [gr-qc].
- [71] J. M. Bowen and J. W. York, Jr., *Phys. Rev. D* **21**, 2047 (1980).
- [72] M. Ansorg, B. Bruegmann, and W. Tichy, *Phys. Rev. D* **70**, 064011 (2004), arXiv:gr-qc/0404056 [gr-qc].
- [73] G. Lovelace, R. Owen, H. P. Pfeiffer, and T. Chu, *Phys. Rev. D* **78**, 084017 (2008), arXiv:0805.4192 [gr-qc].
- [74] H. P. Pfeiffer and J. W. York, Jr., *Phys. Rev. D* **67**, 044022 (2003), arXiv:gr-qc/0207095 [gr-qc].
- [75] H. P. Pfeiffer, L. E. Kidder, M. A. Scheel, and S. A. Teukolsky, *Comput. Phys. Commun.* **152**, 253 (2003), arXiv:gr-qc/0202096 [gr-qc].
- [76] L. Lindblom, M. A. Scheel, L. E. Kidder, R. Owen, and O. Rinne, *Class. Quant. Grav.* **23**, 447 (2006), gr-qc/0512093.
- [77] F. Pretorius, *Phys. Rev. Lett.* **95**, 121101 (2005), arXiv:gr-qc/0507014 [gr-qc].
- [78] H. Friedrich, *Communications in Mathematical Physics* **100**, 525 (1985).
- [79] L. Lindblom and B. Szilágyi, *Phys. Rev. D* **80**, 084019 (2009), arXiv:0904.4873 [gr-qc].
- [80] B. Szilágyi, *Int. J. Mod. Phys. D* **23**, 1430014 (2014), arXiv:1405.3693 [gr-qc].
- [81] D. A. Hemberger, M. A. Scheel, L. E. Kidder, B. Szilágyi, G. Lovelace, N. W. Taylor, and S. A. Teukolsky, *Class. Quant. Grav.* **30**, 115001 (2013), arXiv:1211.6079 [gr-qc].
- [82] M. A. Scheel, M. Giesler, D. A. Hemberger, G. Lovelace, K. Kuper, M. Boyle, B. Szilágyi, and L. E. Kidder, *Class. Quant. Grav.* **32**, 105009 (2015), arXiv:1412.1803 [gr-qc].
- [83] K. Barkett *et al.*, *Phys. Rev. D* **93**, 044064 (2016), arXiv:1509.05782 [gr-qc].
- [84] G. Lovelace *et al.*, *Class. Quant. Grav.* **32**, 065007 (2015), arXiv:1411.7297 [gr-qc].
- [85] <http://www.black-holes.org/waveforms>.
- [86] T. Chu, H. Fong, P. Kumar, H. P. Pfeiffer, M. Boyle, D. A. Hemberger, L. E. Kidder, M. A. Scheel, and B. Szilágyi, *Class. Quant. Grav.* **33**, 165001 (2016), arXiv:1512.06800 [gr-qc].
- [87] J. Blackman, S. E. Field, M. A. Scheel, C. R. Galley, D. A. Hemberger, P. Schmidt, and R. Smith, (2017), arXiv:1701.00550 [gr-qc].
- [88] M. Boyle and A. H. Mroue, *Phys. Rev. D* **80**, 124045 (2009), arXiv:0905.3177 [gr-qc].
- [89] M. Boyle, *Phys. Rev. D* **93**, 084031 (2016), arXiv:1509.00862 [gr-qc].
- [90] M. Hannam, S. Husa, J. G. Baker, M. Boyle, B. Brügmann, T. Chu, N. Dorband, F. Herrmann, I. Hinder, B. J. Kelly, L. E. Kidder, P. Laguna, K. D. Matthews, J. R. van Meter, H. P. Pfeiffer, D. Pollney, C. Reisswig, M. A. Scheel, and D. Shoemaker, *Phys. Rev. D* **79**, 084025 (2009).
- [91] G. Lovelace *et al.*, *Class. Quant. Grav.* **33**, 244002 (2016), arXiv:1607.05377 [gr-qc].
- [92] C. R. Galley and P. Schmidt, (2016), arXiv:1611.07529 [gr-qc].
- [93] P. Schmidt, I. W. Harry, and H. P. Pfeiffer, (2017), LIGO-T1500606, arXiv:1703.01076 [gr-qc].
- [94] “LSC Algorithm Library LAL,” <http://www.lsc-group.phys.uwm.edu/lal>.
- [95] W. G. Anderson, P. R. Brady, J. D. E. Creighton, and E. E. Flanagan, *Phys. Rev. D* **63**, 042003 (2001), arXiv:gr-qc/0008066 [gr-qc].
- [96] K. S. Thorne, in *Three hundred years of gravitation*, edited by S. W. Hawking and W. Israel (Cambridge University Press, Cambridge, 1987) Chap. 9, pp. 330–458.
- [97] K. Cannon, J. Creighton, and T. Creighton, “Injection coordinate system,” http://software.ligo.org/docs/lalsuite/lalsimulation/group___l_a_l_simulation__h.html.
- [98] T. Dal Canton *et al.*, *Phys. Rev. D* **90**, 082004 (2014), arXiv:1405.6731 [gr-qc].
- [99] S. A. Usman *et al.*, *Class. Quant. Grav.* **33**, 215004 (2016), arXiv:1508.02357 [gr-qc].
- [100] A. H. Nitz, I. W. Harry, J. L. Willis, C. M. Biwer, D. A. Brown, L. P. Pekowsky, T. Dal Canton, A. R. Williamson, T. Dent, C. D. Capano, T. J. Massinger, A. K. Lenon, A. Nielsen, and M. Cabero, “PyCBC Software,” <https://github.com/ligo-cbc/pycbc> (2016).
- [101] C. Biwer *et al.*, (2016), arXiv:1612.07864 [astro-ph.IM].
- [102] C. Cutler and E. E. Flanagan, *Phys. Rev. D* **49**, 2658 (1994), arXiv:gr-qc/9402014 [gr-qc].
- [103] B. P. Abbott *et al.* (LIGO Scientific), *Phys. Rev. D* **95**, 062003 (2017), arXiv:1602.03845 [gr-qc].
- [104] A. Buonanno, L. E. Kidder, A. H. Mroue, H. P. Pfeiffer, and A. Taracchini, *Phys. Rev. D* **83**, 104034 (2011), arXiv:1012.1549 [gr-qc].
- [105] S. Husa, M. Hannam, J. A. Gonzalez, U. Sperhake, and B. Bruegmann, *Phys. Rev. D* **77**, 044037 (2008), arXiv:0706.0904 [gr-qc].
- [106] M. Purrer, S. Husa, and M. Hannam, *Phys. Rev. D* **85**, 124051 (2012), arXiv:1203.4258 [gr-qc].
- [107] P. C. Peters, *Phys. Rev.* **136**, B1224 (1964).
- [108] T. Damour, B. R. Iyer, and B. S. Sathyaprakash, *Phys. Rev. D* **57**, 885 (1998), arXiv:gr-qc/9708034 [gr-qc].
- [109] T. Bayes and R. Price, *Phil. Trans. Roy. Soc. Lond.* **53**, 370 (1763).

- [110] E. T. Jaynes, *Probability Theory: The Logic of Science*, edited by G. L. Bretthorst (Cambridge University Press, Cambridge, 2003).
- [111] J. Veitch, V. Raymond, B. Farr, W. Farr, P. Graff, *et al.*, *Phys.Rev.* **D91**, 042003 (2015), [arXiv:1409.7215 \[gr-qc\]](#).
- [112] B. P. Abbott *et al.* (Virgo, LIGO Scientific), *Class. Quant. Grav.* **33**, 134001 (2016), [arXiv:1602.03844 \[gr-qc\]](#).
- [113] W. M. Farr, B. Farr, and T. Littenberg, *Modelling Calibration Errors In CBC Waveforms*, Tech. Rep. LIGO-T1400682 (LIGO Project, 2015).
- [114] J. Aasi *et al.* (LIGO Scientific Collaboration, Virgo Collaboration, NINJA-2 Collaboration), *Class. Quant. Grav.* **31**, 115004 (2014), [arXiv:1401.0939 \[gr-qc\]](#).
- [115] J. Veitch, M. Pürrer, and I. Mandel, *Phys. Rev. Lett.* **115**, 141101 (2015), [arXiv:1503.05953 \[astro-ph.HE\]](#).
- [116] P. B. Graff, A. Buonanno, and B. S. Sathyaprakash, *Phys. Rev.* **D92**, 022002 (2015), [arXiv:1504.04766 \[gr-qc\]](#).
- [117] A. Krolak and B. F. Schutz, *Gen. Rel. Grav.* **19**, 1163 (1987).
- [118] M. Pürrer, M. Hannam, and F. Ohme, *Phys. Rev.* **D93**, 084042 (2016), [arXiv:1512.04955 \[gr-qc\]](#).
- [119] K. Arun, A. Buonanno, G. Faye, and E. Ochsner, *Phys. Rev. D* **79**, 104023 (2009), [arXiv:0810.5336 \[gr-qc\]](#).
- [120] L. S. Finn and D. F. Chernoff, *Phys. Rev.* **D47**, 2198 (1993), [arXiv:gr-qc/9301003 \[gr-qc\]](#).
- [121] V. Raymond and W. Farr, (2014), [arXiv:1402.0053 \[gr-qc\]](#).
- [122] S. Klimenko, S. Mohanty, M. Rakhmanov, and G. Mitselmakher, *Physical Review D* **72**, 122002 (2005).
- [123] P. J. Sutton *et al.*, *New J. Phys.* **12**, 053034 (2010), [arXiv:0908.3665 \[gr-qc\]](#).
- [124] L. Pekowsky, J. Healy, D. Shoemaker, and P. Laguna, *Phys. Rev.* **D87**, 084008 (2013), [arXiv:1210.1891 \[gr-qc\]](#).
- [125] V. Varma, P. Ajith, S. Husa, J. C. Bustillo, M. Hannam, *et al.*, *Phys.Rev.* **D90**, 124004 (2014), [arXiv:1409.2349 \[gr-qc\]](#).
- [126] J. Calderón Bustillo, S. Husa, A. M. Sintes, and M. Pürrer, *Phys. Rev.* **D93**, 084019 (2016), [arXiv:1511.02060 \[gr-qc\]](#).
- [127] C. Capano, Y. Pan, and A. Buonanno, *Phys. Rev.* **D89**, 102003 (2014), [arXiv:1311.1286 \[gr-qc\]](#).
- [128] J. Healy, P. Laguna, L. Pekowsky, and D. Shoemaker, *Phys. Rev.* **D88**, 024034 (2013), [arXiv:1302.6953 \[gr-qc\]](#).
- [129] A. H. Mroue, H. P. Pfeiffer, L. E. Kidder, and S. A. Teukolsky, *Phys. Rev.* **D82**, 124016 (2010), [arXiv:1004.4697 \[gr-qc\]](#).
- [130] D. Tuyenbayev *et al.*, *Class. Quant. Grav.* **34**, 015002 (2017), [arXiv:1608.05134 \[astro-ph.IM\]](#).
- [131] S. Karki *et al.*, *Rev. Sci. Instrum.* **87**, 114503 (2016), [arXiv:1608.05055 \[astro-ph.IM\]](#).
- [132] T. Regge and J. A. Wheeler, *Phys. Rev.* **108**, 1063 (1957).
- [133] F. J. Zerilli, *Phys. Rev. Lett.* **24**, 737 (1970).
- [134] O. Sarbach and M. Tiglio, *Phys. Rev.* **D64**, 084016 (2001), [arXiv:gr-qc/0104061 \[gr-qc\]](#).
- [135] O. Rinne, L. T. Buchman, M. A. Scheel, and H. P. Pfeiffer, *Classical and Quantum Gravity* **26**, 075009 (2009).
- [136] P. Peters and J. Mathews, *Phys.Rev.* **131**, 435 (1963).
- [137] E. A. Huerta *et al.*, *Phys. Rev.* **D95**, 024038 (2017), [arXiv:1609.05933 \[gr-qc\]](#).
- [138] P. Ajith, M. Boyle, D. A. Brown, B. Brügmann, L. T. Buchman, L. Cadonati, M. Campanelli and T. Chu *et al.*, *Class. Quant. Grav.* **29**, 124001 (2012), [arXiv:1201.5319 \[gr-qc\]](#).
- [139] B. S. Sathyaprakash and B. F. Schutz, *Living Reviews in Relativity* **12**, 2 (2009), [arXiv:0903.0338 \[gr-qc\]](#).

Authors

B. P. Abbott,¹ R. Abbott,¹ T. D. Abbott,² M. R. Abernathy,³ F. Acernese,^{4,5} K. Ackley,⁶ C. Adams,⁷ T. Adams,⁸ P. Addesso,⁹ R. X. Adhikari,¹ V. B. Adya,¹⁰ C. Affeldt,¹⁰ M. Agathos,¹¹ K. Agatsuma,¹¹ N. Aggarwal,¹² O. D. Aguiar,¹³ L. Aiello,^{14,15} A. Ain,¹⁶ P. Ajith,¹⁷ B. Allen,^{10,18,19} A. Allocca,^{20,21} P. A. Altin,²² A. Ananyeva,¹ S. B. Anderson,¹ W. G. Anderson,¹⁸ S. Appert,¹ K. Arai,¹ M. C. Araya,¹ J. S. Areeda,²³ N. Arnaud,²⁴ K. G. Arun,²⁵ S. Ascenzi,^{26,15} G. Ashton,¹⁰ M. Ast,²⁷ S. M. Aston,⁷ P. Astone,²⁸ P. Aufmuth,¹⁹ C. Aulbert,¹⁰ A. Avila-Alvarez,²³ S. Babak,²⁹ P. Bacon,³⁰ M. K. M. Bader,¹¹ P. T. Baker,³¹ F. Baldaccini,^{32,33} G. Ballardini,³⁴ S. W. Ballmer,³⁵ J. C. Barayoga,¹ S. E. Barclay,³⁶ B. C. Barish,¹ D. Barker,³⁷ F. Barone,^{4,5} B. Barr,³⁶ L. Barsotti,¹² M. Barsuglia,³⁰ D. Barta,³⁸ J. Bartlett,³⁷ I. Bartos,³⁹ R. Bassiri,⁴⁰ A. Basti,^{20,21} J. C. Batch,³⁷ C. Baune,¹⁰ V. Bavagadda,³⁴ M. Bazzan,^{41,42} C. Beer,¹⁰ M. Bejger,⁴³ I. Belahcene,²⁴ M. Belgin,⁴⁴ A. S. Bell,³⁶ B. K. Berger,¹ G. Bergmann,¹⁰ C. P. L. Berry,⁴⁵ D. Bersanetti,^{46,47} A. Bertolini,¹¹ J. Betzwieser,⁷ S. Bhagwat,³⁵ R. Bhandare,⁴⁸ I. A. Bilenko,⁴⁹ G. Billingsley,¹ C. R. Billman,⁶ J. Birch,⁷ R. Birney,⁵⁰ O. Birnholtz,¹⁰ S. Biscans,^{12,1} A. Bisht,¹⁹ M. Bitossi,³⁴ C. Biwer,³⁵ M. A. Bizouard,²⁴ J. K. Blackburn,¹ J. Blackman,⁵¹ C. D. Blair,⁵² D. G. Blair,⁵² R. M. Blair,³⁷ S. Bloemen,⁵³ O. Bock,¹⁰ M. Boer,⁵⁴ G. Bogaert,⁵⁴ A. Bohe,²⁹ F. Bondu,⁵⁵ R. Bonnand,⁸ B. A. Boom,¹¹ R. Bork,¹ V. Boschi,^{20,21} S. Bose,^{56,16} Y. Bouffanais,³⁰ A. Bozzi,³⁴ C. Bradaschia,²¹ P. R. Brady,¹⁸ V. B. Braginsky,⁴⁹ M. Branchesi,^{57,58} J. E. Brau,⁵⁹ T. Briant,⁶⁰ A. Brillet,⁵⁴ M. Brinkmann,¹⁰ V. Brisson,²⁴ P. Brockill,¹⁸ J. E. Broida,⁶¹ A. F. Brooks,¹ D. A. Brown,³⁵ D. D. Brown,⁴⁵ N. M. Brown,¹² S. Brunett,¹ C. C. Buchanan,² A. Buikema,¹² T. Bulik,⁶² H. J. Bulten,^{63,11} A. Buonanno,^{29,64} D. Buskulic,⁸ C. Buy,³⁰ R. L. Byer,⁴⁰ M. Cabero,¹⁰ L. Cadonati,⁴⁴ G. Cagnoli,^{65,66} C. Cahillane,¹ J. Calderón Bustillo,⁴⁴ T. A. Callister,¹ E. Calloni,^{67,5} J. B. Camp,⁶⁸ K. C. Cannon,⁶⁹ H. Cao,⁷⁰ J. Cao,⁷¹ C. D. Capano,¹⁰ E. Capocasa,³⁰ F. Carbognani,³⁴ S. Caride,⁷² J. Casanueva Diaz,²⁴ C. Casentini,^{26,15} S. Caudill,¹⁸ M. Cavaglià,⁷³ F. Cavalier,²⁴ R. Cavalieri,³⁴ G. Cella,²¹ C. B. Cepeda,¹ L. Cerboni Baiardi,^{57,58} G. Cerretani,^{20,21} E. Cesarini,^{26,15} S. J. Chamberlin,⁷⁴ M. Chan,³⁶ S. Chao,⁷⁵ P. Charlton,⁷⁶ E. Chassande-Mottin,³⁰ B. D. Cheeseboro,³¹ H. Y. Chen,⁷⁷ Y. Chen,⁵¹ H.-P. Cheng,⁶ A. Chincarini,⁴⁷ A. Chiummo,³⁴ T. Chmiel,⁷⁸ H. S. Cho,⁷⁹ M. Cho,⁶⁴ J. H. Chow,²² N. Christensen,⁶¹ Q. Chu,⁵² A. J. K. Chua,⁸⁰ S. Chua,⁶⁰ S. Chung,⁵² G. Ciani,⁶ F. Clara,³⁷ J. A. Clark,⁴⁴ F. Cleva,⁵⁴ C. Cocchieri,⁷³ E. Coccia,^{14,15} P.-F. Cohadon,⁶⁰ A. Colla,^{81,28} C. G. Collette,⁸² L. Cominsky,⁸³ M. M. Constancio Jr.,¹³ L. Conti,⁴² S. J. Cooper,⁴⁵ T. R. Corbitt,² N. Cornish,⁸⁴ A. Corsi,⁷² S. Cortese,³⁴ C. A. Costa,¹³ M. W. Coughlin,⁶¹ S. B. Coughlin,⁸⁵ J.-P. Coulon,⁵⁴ S. T. Countryman,³⁹ P. Couvares,¹ P. B. Covas,⁸⁶ E. E. Cowan,⁴⁴ D. M. Coward,⁵² M. J. Coward,⁷ D. C. Coyne,¹ R. Coyne,⁷² J. D. E. Creighton,¹⁸ T. D. Creighton,⁸⁷ J. Cripe,² S. G. Crowder,⁸⁸ T. J. Cullen,²³ A. Cumming,³⁶ L. Cunningham,³⁶ E. Cuoco,³⁴ T. Dal Canton,⁶⁸ S. L. Danilishin,³⁶ S. D'Antonio,¹⁵ K. Danzmann,^{19,10} A. Dasgupta,⁸⁹ C. F. Da Silva Costa,⁶ V. Dattilo,³⁴ I. Dave,⁴⁸ M. Davier,²⁴ G. S. Davies,³⁶ D. Davis,³⁵ E. J. Daw,⁹⁰ B. Day,⁴⁴ R. Day,³⁴ S. De,³⁵ D. DeBra,⁴⁰ G. Debreczeni,³⁸ J. Degallaix,⁶⁵ M. De Laurentis,^{67,5} S. Deléglise,⁶⁰ W. Del Pozzo,⁴⁵ T. Denker,¹⁰ T. Dent,¹⁰ V. Dergachev,²⁹ R. De Rosa,^{67,5} R. T. DeRosa,⁷ R. DeSalvo,⁹¹ J. Devenson,⁵⁰ R. C. Devine,³¹ S. Dhurandhar,¹⁶ M. C. Díaz,⁸⁷ L. Di Fiore,⁵ M. Di Giovanni,^{92,93} T. Di Girolamo,^{67,5} A. Di Lieto,^{20,21} S. Di Pace,^{81,28} I. Di Palma,^{29,81,28} A. Di Virgilio,²¹ Z. Doctor,⁷⁷ V. Dolique,⁶⁵ F. Donovan,¹² K. L. Dooley,⁷³ S. Doravari,¹⁰ I. Dorrington,⁹⁴ R. Douglas,³⁶ M. Dovalé Álvarez,⁴⁵ T. P. Downes,¹⁸ M. Drago,¹⁰ R. W. P. Drever,^{**} J. C. Driggers,³⁷ Z. Du,⁷¹ M. Ducrot,⁸ S. E. Dwyer,³⁷ T. B. Edo,⁹⁰ M. C. Edwards,⁶¹ A. Effler,⁷ H.-B. Eggenstein,¹⁰ P. Ehrens,¹ J. Eichholz,¹ S. S. Eikenberry,⁶ R. A. Eisenstein,¹² R. C. Essick,¹² Z. Etienne,³¹ T. Etzel,¹ M. Evans,¹² T. M. Evans,⁷ R. Everett,⁷⁴ M. Factourovich,³⁹ V. Fafone,^{26,15,14} H. Fair,³⁵ S. Fairhurst,⁹⁴ X. Fan,⁷¹ S. Farinon,⁴⁷ B. Farr,⁷⁷ W. M. Farr,⁴⁵ E. J. Fauchon-Jones,⁹⁴ M. Favata,⁹⁵ M. Fays,⁹⁴ H. Fehrmann,¹⁰ M. M. Fejer,⁴⁰ A. Fernández Galiana,¹² I. Ferrante,^{20,21} E. C. Ferreira,¹³ F. Ferrini,³⁴ F. Fidecaro,^{20,21} I. Fiori,³⁴ D. Fiorucci,³⁰ R. P. Fisher,³⁵ R. Flaminio,^{65,96} M. Fletcher,³⁶ H. Fong,⁹⁷ S. S. Forsyth,⁴⁴ J.-D. Fournier,⁵⁴ S. Frasca,^{81,28} F. Frasconi,²¹ Z. Frei,⁹⁸ A. Freise,⁴⁵ R. Frey,⁵⁹ V. Frey,²⁴ E. M. Fries,¹ P. Fritschel,¹² V. V. Frolov,⁷ P. Fulda,^{6,68} M. Fyffe,⁷ H. Gabbard,¹⁰ B. U. Gadre,¹⁶ S. M. Gaebel,⁴⁵ J. R. Gair,⁹⁹ L. Gammaitoni,³² S. G. Gaonkar,¹⁶ F. Garufi,^{67,5} G. Gaur,¹⁰⁰ V. Gayathri,¹⁰¹ N. Gehrels,⁶⁸ G. Gemme,⁴⁷ E. Genin,³⁴ A. Gennai,²¹ J. George,⁴⁸ L. Gergely,¹⁰² V. Germain,⁸ S. Ghonge,¹⁷ Abhirup Ghosh,¹⁷ Archisman Ghosh,^{11,17} S. Ghosh,^{53,11} J. A. Giaime,^{2,7} K. D. Giardina,⁷ A. Giazotto,²¹ K. Gill,¹⁰³ A. Glaefke,³⁶ E. Goetz,¹⁰ R. Goetz,⁶ L. Gondan,⁹⁸ G. González,² J. M. Gonzalez Castro,^{20,21} A. Gopakumar,¹⁰⁴ M. L. Gorodetsky,⁴⁹ S. E. Gossan,¹ M. Gosselin,³⁴ R. Gouaty,⁸ A. Grado,^{105,5} C. Graef,³⁶ M. Granata,⁶⁵ A. Grant,³⁶ S. Gras,¹² C. Gray,³⁷ G. Greco,^{57,58} A. C. Green,⁴⁵ P. Groot,⁵³ H. Grote,¹⁰ S. Grunewald,²⁹ G. M. Guidi,^{57,58} X. Guo,⁷¹ A. Gupta,¹⁶ M. K. Gupta,⁸⁹ K. E. Gushwa,¹ E. K. Gustafson,¹ R. Gustafson,¹⁰⁶ J. J. Hacker,²³ B. R. Hall,⁵⁶ E. D. Hall,¹ G. Hammond,³⁶ M. Haney,¹⁰⁴ M. M. Hanke,¹⁰ J. Hanks,³⁷ C. Hanna,⁷⁴ M. D. Hannam,⁹⁴ J. Hanson,⁷ T. Hardwick,² J. Harms,^{57,58} G. M. Harry,³ I. W. Harry,²⁹ M. J. Hart,³⁶ M. T. Hartman,⁶ C.-J. Haster,^{45,97} K. Haughian,³⁶ J. Healy,¹⁰⁷ A. Heidmann,⁶⁰ M. C. Heintze,⁷ H. Heitmann,⁵⁴ P. Hello,²⁴ G. Hemming,³⁴ M. Hendry,³⁶ I. S. Heng,³⁶ J. Hennig,³⁶ J. Henry,¹⁰⁷ A. W. Heptonstall,¹ M. Heurs,^{10,19} S. Hild,³⁶ D. Hoak,³⁴ D. Hofman,⁶⁵ K. Holt,⁷ D. E. Holz,⁷⁷ P. Hopkins,⁹⁴ J. Hough,³⁶ E. A. Houston,³⁶ E. J. Howell,⁵² Y. M. Hu,¹⁰ E. A. Huerta,¹⁰⁸ D. Huet,²⁴ B. Hughey,¹⁰³ S. Husa,⁸⁶ S. H. Huttner,³⁶ T. Huynh-Dinh,⁷ N. Indik,¹⁰ D. R. Ingram,³⁷ R. Inta,⁷² H. N. Isa,³⁶ J.-M. Isac,⁶⁰ M. Isi,¹ T. Isogai,¹² B. R. Iyer,¹⁷ K. Izumi,³⁷ T. Jacqmin,⁶⁰ K. Jani,⁴⁴ P. Jaranowski,¹⁰⁹ S. Jawahar,¹¹⁰ F. Jiménez-Forteza,⁸⁶ W. W. Johnson,² D. I. Jones,¹¹¹ R. Jones,³⁶ R. J. G. Jonker,¹¹ L. Ju,⁵² J. Junker,¹⁰ C. V. Kalaghatgi,⁹⁴ V. Kalogera,⁸⁵ S. Kandhasamy,⁷³ G. Kang,⁷⁹ J. B. Kanner,¹ S. Karki,⁵⁹ K. S. Karvinen,¹⁰ M. Kasprzak,² E. Katsavounidis,¹² W. Katzman,⁷ S. Kaufer,¹⁹ T. Kaur,⁵² K. Kawabe,³⁷ F. Kéfélian,⁵⁴ D. Keitel,⁸⁶ D. B. Kelley,³⁵ R. Kennedy,⁹⁰ J. S. Key,¹¹² F. Y. Khalili,⁴⁹ I. Khan,¹⁴ S. Khan,⁹⁴ Z. Khan,⁸⁹ E. A. Khazanov,¹¹³ N. Kijbunchoo,³⁷ Chunglee Kim,¹¹⁴ J. C. Kim,¹¹⁵ Whansun Kim,¹¹⁶ W. Kim,⁷⁰ Y.-M. Kim,^{117,114} S. J. Kimbrell,⁴⁴ E. J. King,⁷⁰ P. J. King,³⁷ R. Kirchhoff,¹⁰ J. S. Kissel,³⁷ B. Klein,⁸⁵ L. Kleybolte,²⁷ S. Klimenko,⁶ P. Koch,¹⁰ S. M. Koehlenbeck,¹⁰ S. Koley,¹¹ V. Kondrashov,¹ A. Kontos,¹² M. Korobko,²⁷ W. Z. Korth,¹ I. Kowalska,⁶²

D. B. Kozak,¹ C. Krämer,¹⁰ V. Kringel,¹⁰ B. Krishnan,¹⁰ A. Królak,^{118,119} G. Kuehn,¹⁰ P. Kumar,⁹⁷ R. Kumar,⁸⁹ L. Kuo,⁷⁵ A. Kutynia,¹¹⁸ B. D. Lackey,^{29,35} M. Landry,³⁷ R. N. Lang,¹⁸ J. Lange,¹⁰⁷ B. Lantz,⁴⁰ R. K. Lanza,¹² A. Lartaux-Vollard,²⁴ P. D. Lasky,¹²⁰ M. Laxen,⁷ A. Lazzarini,¹ C. Lazzaro,⁴² P. Leaci,^{81,28} S. Leavey,³⁶ E. O. Lebigot,³⁰ C. H. Lee,¹¹⁷ H. K. Lee,¹²¹ H. M. Lee,¹¹⁴ K. Lee,³⁶ J. Lehmann,¹⁰ A. Lenon,³¹ M. Leonardi,^{92,93} J. R. Leong,¹⁰ N. Leroy,²⁴ N. Letendre,⁸ Y. Levin,¹²⁰ T. G. F. Li,¹²² A. Libson,¹² T. B. Littenberg,¹²³ J. Liu,⁵² N. A. Lockerbie,¹¹⁰ A. L. Lombardi,⁴⁴ L. T. London,⁹⁴ J. E. Lord,³⁵ M. Lorenzini,^{14,15} V. Lorette,¹²⁴ M. Lormand,⁷ G. Losurdo,²¹ J. D. Lough,^{10,19} G. Lovelace,²³ H. Lück,^{19,10} A. P. Lundgren,¹⁰ R. Lynch,¹² Y. Ma,⁵¹ S. Macfoy,⁵⁰ B. Machenschalk,¹⁰ M. MacInnis,¹² D. M. Macleod,² F. Magaña-Sandoval,³⁵ E. Majorana,²⁸ I. Maksimovic,¹²⁴ V. Malvezzi,^{26,15} N. Man,⁵⁴ V. Mandic,¹²⁵ V. Mangano,³⁶ G. L. Mansell,²² M. Manske,¹⁸ M. Mantovani,³⁴ F. Marchesoni,^{126,33} F. Marion,⁸ S. Márka,³⁹ Z. Márka,³⁹ A. S. Markosyan,⁴⁰ E. Maros,¹ F. Martelli,^{57,58} L. Martellini,⁵⁴ I. W. Martin,³⁶ D. V. Martynov,¹² K. Mason,¹² A. Masserot,⁸ T. J. Massinger,¹ M. Masso-Reid,³⁶ S. Mastrogiovanni,^{81,28} F. Matichard,^{12,1} L. Matone,³⁹ N. Mavalvala,¹² N. Mazumder,⁵⁶ R. McCarthy,³⁷ D. E. McClelland,²² S. McCormick,⁷ C. McGrath,¹⁸ S. C. McGuire,¹²⁷ G. McIntyre,¹ J. McIver,¹ D. J. McManus,²² T. McRae,²² S. T. McWilliams,³¹ D. Meacher,^{54,74} G. D. Meadors,^{29,10} J. Meidam,¹¹ A. Melatos,¹²⁸ G. Mendell,³⁷ D. Mendoza-Gandara,¹⁰ R. A. Mercer,¹⁸ E. L. Merilh,³⁷ M. Merzougui,⁵⁴ S. Meshkov,¹ C. Messenger,³⁶ C. Messick,⁷⁴ R. Metzdrorf,⁶⁰ P. M. Meyers,¹²⁵ F. Mezzani,^{28,81} H. Miao,⁴⁵ C. Michel,⁶⁵ H. Middleton,⁴⁵ E. E. Mikhailov,¹²⁹ L. Milano,^{67,5} A. L. Miller,^{6,81,28} A. Miller,⁸⁵ B. B. Miller,⁸⁵ J. Miller,¹² M. Millhouse,⁸⁴ Y. Minenkov,¹⁵ J. Ming,²⁹ S. Mirshekari,¹³⁰ C. Mishra,¹⁷ S. Mitra,¹⁶ V. P. Mitrofanov,⁴⁹ G. Mitselmakher,⁶ R. Mittleman,¹² A. Moggi,²¹ M. Mohan,³⁴ S. R. P. Mohapatra,¹² M. Montani,^{57,58} B. C. Moore,⁹⁵ C. J. Moore,⁸⁰ D. Moraru,³⁷ G. Moreno,³⁷ S. R. Morris,⁸⁷ B. Mours,⁸ C. M. Mow-Lowry,⁴⁵ G. Mueller,⁶ A. W. Muir,⁹⁴ Arunava Mukherjee,¹⁷ D. Mukherjee,¹⁸ S. Mukherjee,⁸⁷ N. Mukund,¹⁶ A. Mullavey,⁷ J. Munch,⁷⁰ E. A. M. Muniz,²³ P. G. Murray,³⁶ A. Mytidis,⁶ K. Napier,⁴⁴ I. Nardecchia,^{26,15} L. Naticchioni,^{81,28} G. Nelemans,^{53,11} T. J. N. Nelson,⁷ M. Neri,^{46,47} M. Nery,¹⁰ A. Neunzert,¹⁰⁶ J. M. Newport,³ G. Newton,³⁶ T. T. Nguyen,²² A. B. Nielsen,¹⁰ S. Nissanke,^{53,11} A. Nitz,¹⁰ A. Noack,¹⁰ F. Nocera,³⁴ D. Nolting,⁷ M. E. N. Normandin,⁸⁷ L. K. Nuttall,³⁵ J. Oberling,³⁷ E. Ochsner,¹⁸ E. Oelker,¹² G. H. Ogin,¹³¹ J. J. Oh,¹¹⁶ S. H. Oh,¹¹⁶ F. Ohme,^{94,10} M. Oliver,⁸⁶ P. Oppermann,¹⁰ Richard J. Oram,⁷ B. O'Reilly,⁷ R. O'Shaughnessy,¹⁰⁷ D. J. Ottaway,⁷⁰ H. Overmier,⁷ B. J. Owen,⁷² A. E. Pace,⁷⁴ J. Page,¹²³ A. Pai,¹⁰¹ S. A. Pai,⁴⁸ J. R. Palamos,⁵⁹ O. Palashov,¹¹³ C. Palomba,²⁸ A. Pal-Singh,²⁷ H. Pan,⁷⁵ C. Pankow,⁸⁵ F. Pannarale,⁹⁴ B. C. Pant,⁴⁸ F. Paoletti,^{34,21} A. Paoli,³⁴ M. A. Papa,^{29,18,10} H. R. Paris,⁴⁰ W. Parker,⁷ D. Pascucci,³⁶ A. Pasqualetti,³⁴ R. Passaquieti,^{20,21} D. Passuello,²¹ B. Patricelli,^{20,21} B. L. Pearlstone,³⁶ M. Pedraza,¹ R. Pedurand,^{65,132} L. Pekowsky,³⁵ A. Pele,⁷ S. Penn,¹³³ C. J. Perez,³⁷ A. Perreca,¹ L. M. Perri,⁸⁵ H. P. Pfeiffer,⁹⁷ M. Phelps,³⁶ O. J. Piccinni,^{81,28} M. Pichot,⁵⁴ F. Piergiovanni,^{57,58} V. Pierro,⁹ G. Pillant,³⁴ L. Pinard,⁶⁵ I. M. Pinto,⁹ M. Pitkin,³⁶ M. Poe,¹⁸ R. Poggiani,^{20,21} P. Popolizio,³⁴ A. Post,¹⁰ J. Powell,³⁶ J. Prasad,¹⁶ J. W. W. Pratt,¹⁰³ V. Predoi,⁹⁴ T. Prestegard,^{125,18} M. Prijatelj,^{10,34} M. Principe,⁹ S. Privitera,²⁹ G. A. Prodi,^{92,93} L. G. Prokhorov,⁴⁹ O. Puncken,¹⁰ M. Punturo,³³ P. Puppo,²⁸ M. Pürner,²⁹ H. Qi,¹⁸ J. Qin,⁵² S. Qiu,¹²⁰ V. Quetschke,⁸⁷ E. A. Quintero,¹ R. Quitzow-James,⁵⁹ F. J. Raab,³⁷ D. S. Rabeling,²² H. Radkins,³⁷ P. Raffai,⁹⁸ S. Raja,⁴⁸ C. Rajan,⁴⁸ M. Rakhmanov,⁸⁷ P. Rapagnani,^{81,28} V. Raymond,²⁹ M. Razzano,^{20,21} V. Re,²⁶ J. Read,²³ T. Regimbau,⁵⁴ L. Rei,⁴⁷ S. Reid,⁵⁰ D. H. Reitze,^{1,6} H. Rew,¹²⁹ S. D. Reyes,³⁵ E. Rhoades,¹⁰³ F. Ricci,^{81,28} K. Riles,¹⁰⁶ M. Rizzo,¹⁰⁷ N. A. Robertson,^{1,36} R. Robie,³⁶ F. Robinet,²⁴ A. Rocchi,¹⁵ L. Rolland,⁸ J. G. Rollins,¹ V. J. Roma,⁵⁹ J. D. Romano,⁸⁷ R. Romano,^{4,5} J. H. Romie,⁷ D. Rosińska,^{134,43} S. Rowan,³⁶ A. Rüdiger,¹⁰ P. Ruggi,³⁴ K. Ryan,³⁷ S. Sachdev,¹ T. Sadecki,³⁷ L. Sadeghian,¹⁸ M. Sakellariadou,¹³⁵ L. Salconi,³⁴ M. Saleem,¹⁰¹ F. Salemi,¹⁰ A. Samajdar,¹³⁶ L. Sammut,¹²⁰ L. M. Sampson,⁸⁵ E. J. Sanchez,¹ V. Sandberg,³⁷ J. R. Sanders,³⁵ B. Sassolas,⁶⁵ B. S. Sathyaprakash,^{74,94} P. R. Saulson,³⁵ O. Sauter,¹⁰⁶ R. L. Savage,³⁷ A. Sawadsky,¹⁹ P. Schale,⁵⁹ J. Scheuer,⁸⁵ E. Schmidt,¹⁰³ J. Schmidt,¹⁰ P. Schmidt,^{1,51} R. Schnabel,²⁷ R. M. S. Schofield,⁵⁹ A. Schönbeck,²⁷ E. Schreiber,¹⁰ D. Schuette,^{10,19} B. F. Schutz,^{94,29} S. G. Schwalbe,¹⁰³ J. Scott,³⁶ S. M. Scott,²² D. Sellers,⁷ A. S. Sengupta,¹³⁷ D. Sentenac,³⁴ V. Sequino,^{26,15} A. Sergeev,¹¹³ Y. Setyawati,^{53,11} D. A. Shaddock,²² T. J. Shaffer,³⁷ M. S. Shahriar,⁸⁵ B. Shapiro,⁴⁰ P. Shawhan,⁶⁴ A. Sheperd,¹⁸ D. H. Shoemaker,¹² D. M. Shoemaker,⁴⁴ K. Siellez,⁴⁴ X. Siemens,¹⁸ M. Sieniawska,⁴³ D. Sigg,³⁷ A. D. Silva,¹³ A. Singer,¹ L. P. Singer,⁶⁸ A. Singh,^{29,10,19} R. Singh,² A. Singhal,¹⁴ A. M. Sintes,⁸⁶ B. J. J. Slagmolen,²² B. Smith,⁷ J. R. Smith,²³ R. J. E. Smith,¹ E. J. Son,¹¹⁶ B. Sorazu,³⁶ F. Sorrentino,⁴⁷ T. Souradeep,¹⁶ A. P. Spencer,³⁶ A. K. Srivastava,⁸⁹ A. Staley,³⁹ M. Steinke,¹⁰ J. Steinlechner,³⁶ S. Steinlechner,^{27,36} D. Steinmeyer,^{10,19} B. C. Stephens,¹⁸ S. P. Stevenson,⁴⁵ R. Stone,⁸⁷ K. A. Strain,³⁶ N. Straniero,⁶⁵ G. Stratta,^{57,58} S. E. Strigin,⁴⁹ R. Sturani,¹³⁰ A. L. Stuver,⁷ T. Z. Summerscales,¹³⁸ L. Sun,¹²⁸ S. Sunil,⁸⁹ P. J. Sutton,⁹⁴ B. L. Swinkels,³⁴ M. J. Szczepańczyk,¹⁰³ M. Tacca,³⁰ D. B. Talukder,⁵⁹ D. B. Tanner,⁶ M. Tápai,¹⁰² A. Taracchini,²⁹ R. Taylor,¹ T. Theeg,¹⁰ E. G. Thomas,⁴⁵ M. Thomas,⁷ P. Thomas,³⁷ K. A. Thorne,⁷ E. Thrane,¹²⁰ T. Tippens,⁴⁴ S. Tiwari,^{14,93} V. Tiwari,⁹⁴ K. V. Tokmakov,¹¹⁰ K. Toland,³⁶ C. Tomlinson,⁹⁰ M. Tonelli,^{20,21} Z. Tornasi,³⁶ C. I. Torrie,¹ D. Töyrä,⁴⁵ F. Travasso,^{32,33} G. Traylor,⁷ D. Trifiro,⁷³ J. Trinastic,⁶ M. C. Tringali,^{92,93} L. Trozzo,^{139,21} M. Tse,¹² R. Tso,¹ M. Turconi,⁵⁴ D. Tuyenbayev,⁸⁷ D. Ugolini,¹⁴⁰ C. S. Unnikrishnan,¹⁰⁴ A. L. Urban,¹ S. A. Usman,⁹⁴ H. Vahlbruch,¹⁹ G. Vajente,¹ G. Valdes,⁸⁷ N. van Bakel,¹¹ M. van Beuzekom,¹¹ J. F. J. van den Brand,^{63,11} C. Van Den Broeck,¹¹ D. C. Vander-Hyde,³⁵ L. van der Schaaf,¹¹ J. V. van Heijningen,¹¹ A. A. van Veggel,³⁶ M. Vardaro,^{41,42} V. Varma,⁵¹ S. Vass,¹ M. Vasúth,³⁸ A. Vecchio,⁴⁵ G. Vedovato,⁴² J. Veitch,⁴⁵ P. J. Veitch,⁷⁰ K. Venkateswara,¹⁴¹ G. Venugopalan,¹ D. Verkindt,⁸ F. Vetrano,^{57,58} A. Viceré,^{57,58} A. D. Viets,¹⁸ S. Vinciguerra,⁴⁵ D. J. Vine,⁵⁰ J.-Y. Vinet,⁵⁴ S. Vitale,¹² T. Vo,³⁵ H. Vocca,^{32,33} C. Vorvick,³⁷ D. V. Voss,⁶ W. D. Vousden,⁴⁵ S. P. Vyatchanin,⁴⁹ A. R. Wade,¹ L. E. Wade,⁷⁸ M. Wade,⁷⁸ M. Walker,² L. Wallace,¹ S. Walsh,^{29,10} G. Wang,^{14,58} H. Wang,⁴⁵ M. Wang,⁴⁵ Y. Wang,⁵² R. L. Ward,²² J. Warner,³⁷ M. Was,⁸ J. Watchi,⁸² B. Weaver,³⁷ L.-W. Wei,⁵⁴ M. Weinert,¹⁰ A. J. Weinstein,¹ R. Weiss,¹² L. Wen,⁵² P. Weßels,¹⁰ T. Westphal,¹⁰ K. Wette,¹⁰ J. T. Whelan,¹⁰⁷ B. F. Whiting,⁶

C. Whittle,¹²⁰ D. Williams,³⁶ R. D. Williams,¹ A. R. Williamson,⁹⁴ J. L. Willis,¹⁴² B. Willke,^{19,10} M. H. Wimmer,^{10,19} W. Winkler,¹⁰ C. C. Wipf,¹ H. Wittel,^{10,19} G. Woan,³⁶ J. Woehler,¹⁰ J. Worden,³⁷ J. L. Wright,³⁶ D. S. Wu,¹⁰ G. Wu,⁷ W. Yam,¹² H. Yamamoto,¹ C. C. Yancey,⁶⁴ M. J. Yap,²² Hang Yu,¹² Haocun Yu,¹² M. Yvert,⁸ A. Zadrożny,¹¹⁸ L. Zangrando,⁴² M. Zanolin,¹⁰³ J.-P. Zendri,⁴² M. Zevin,⁸⁵ L. Zhang,¹ M. Zhang,¹²⁹ T. Zhang,³⁶ Y. Zhang,¹⁰⁷ C. Zhao,⁵² M. Zhou,⁸⁵ Z. Zhou,⁸⁵ S. J. Zhu,^{29,10} X. J. Zhu,⁵² M. E. Zucker,^{1,12} and J. Zweizig¹

(LIGO Scientific Collaboration and Virgo Collaboration)

M. Boyle,¹⁴³ T. Chu,⁹⁷ D. Hemberger,⁵¹ I. Hinder,²⁹ L. E. Kidder,¹⁴³ S. Ossokine,²⁹ M. Scheel,⁵¹ B. Szilagyi,⁵¹ S. Teukolsky,¹⁴³ and A. Vano Vinuales⁹⁴

*Deceased, March 2016. **Deceased, March 2017.

¹LIGO, California Institute of Technology, Pasadena, CA 91125, USA

²Louisiana State University, Baton Rouge, LA 70803, USA

³American University, Washington, D.C. 20016, USA

⁴Università di Salerno, Fisciano, I-84084 Salerno, Italy

⁵INFN, Sezione di Napoli, Complesso Universitario di Monte S. Angelo, I-80126 Napoli, Italy

⁶University of Florida, Gainesville, FL 32611, USA

⁷LIGO Livingston Observatory, Livingston, LA 70754, USA

⁸Laboratoire d'Annecy-le-Vieux de Physique des Particules (LAPP), Université Savoie Mont Blanc, CNRS/IN2P3, F-74941 Annecy-le-Vieux, France

⁹University of Sannio at Benevento, I-82100 Benevento, Italy and INFN, Sezione di Napoli, I-80100 Napoli, Italy

¹⁰Albert-Einstein-Institut, Max-Planck-Institut für Gravitationsphysik, D-30167 Hannover, Germany

¹¹Nikhef, Science Park, 1098 XG Amsterdam, The Netherlands

¹²LIGO, Massachusetts Institute of Technology, Cambridge, MA 02139, USA

¹³Instituto Nacional de Pesquisas Espaciais, 12227-010 São José dos Campos, São Paulo, Brazil

¹⁴INFN, Gran Sasso Science Institute, I-67100 L'Aquila, Italy

¹⁵INFN, Sezione di Roma Tor Vergata, I-00133 Roma, Italy

¹⁶Inter-University Centre for Astronomy and Astrophysics, Pune 411007, India

¹⁷International Centre for Theoretical Sciences, Tata Institute of Fundamental Research, Bengaluru 560089, India

¹⁸University of Wisconsin-Milwaukee, Milwaukee, WI 53201, USA

¹⁹Leibniz Universität Hannover, D-30167 Hannover, Germany

²⁰Università di Pisa, I-56127 Pisa, Italy

²¹INFN, Sezione di Pisa, I-56127 Pisa, Italy

²²Australian National University, Canberra, Australian Capital Territory 0200, Australia

²³California State University Fullerton, Fullerton, CA 92831, USA

²⁴LAL, Univ. Paris-Sud, CNRS/IN2P3, Université Paris-Saclay, F-91898 Orsay, France

²⁵Chennai Mathematical Institute, Chennai 603103, India

²⁶Università di Roma Tor Vergata, I-00133 Roma, Italy

²⁷Universität Hamburg, D-22761 Hamburg, Germany

²⁸INFN, Sezione di Roma, I-00185 Roma, Italy

²⁹Albert-Einstein-Institut, Max-Planck-Institut für Gravitationsphysik, D-14476 Potsdam-Golm, Germany

³⁰APC, AstroParticule et Cosmologie, Université Paris Diderot, CNRS/IN2P3, CEA/Irfu, Observatoire de Paris, Sorbonne Paris Cité, F-75205 Paris Cedex 13, France

³¹West Virginia University, Morgantown, WV 26506, USA

³²Università di Perugia, I-06123 Perugia, Italy

³³INFN, Sezione di Perugia, I-06123 Perugia, Italy

³⁴European Gravitational Observatory (EGO), I-56021 Cascina, Pisa, Italy

³⁵Syracuse University, Syracuse, NY 13244, USA

³⁶SUPA, University of Glasgow, Glasgow G12 8QQ, United Kingdom

³⁷LIGO Hanford Observatory, Richland, WA 99352, USA

³⁸Wigner RCP, RMKI, H-1121 Budapest, Konkoly Thege Miklós út 29-33, Hungary

³⁹Columbia University, New York, NY 10027, USA

⁴⁰Stanford University, Stanford, CA 94305, USA

⁴¹Università di Padova, Dipartimento di Fisica e Astronomia, I-35131 Padova, Italy

⁴²INFN, Sezione di Padova, I-35131 Padova, Italy

⁴³Nicolaus Copernicus Astronomical Center, Polish Academy of Sciences, 00-716, Warsaw, Poland

⁴⁴Center for Relativistic Astrophysics and School of Physics, Georgia Institute of Technology, Atlanta, GA 30332, USA

- ⁴⁵University of Birmingham, Birmingham B15 2TT, United Kingdom
- ⁴⁶Università degli Studi di Genova, I-16146 Genova, Italy
- ⁴⁷INFN, Sezione di Genova, I-16146 Genova, Italy
- ⁴⁸RRCAT, Indore MP 452013, India
- ⁴⁹Faculty of Physics, Lomonosov Moscow State University, Moscow 119991, Russia
- ⁵⁰SUPA, University of the West of Scotland, Paisley PA1 2BE, United Kingdom
- ⁵¹Caltech CaRT, Pasadena, CA 91125, USA
- ⁵²University of Western Australia, Crawley, Western Australia 6009, Australia
- ⁵³Department of Astrophysics/IMAPP, Radboud University Nijmegen, P.O. Box 9010, 6500 GL Nijmegen, The Netherlands
- ⁵⁴Artemis, Université Côte d’Azur, CNRS, Observatoire Côte d’Azur, CS 34229, F-06304 Nice Cedex 4, France
- ⁵⁵Institut de Physique de Rennes, CNRS, Université de Rennes 1, F-35042 Rennes, France
- ⁵⁶Washington State University, Pullman, WA 99164, USA
- ⁵⁷Università degli Studi di Urbino ‘Carlo Bo’, I-61029 Urbino, Italy
- ⁵⁸INFN, Sezione di Firenze, I-50019 Sesto Fiorentino, Firenze, Italy
- ⁵⁹University of Oregon, Eugene, OR 97403, USA
- ⁶⁰Laboratoire Kastler Brossel, UPMC-Sorbonne Universités, CNRS, ENS-PSL Research University, Collège de France, F-75005 Paris, France
- ⁶¹Carleton College, Northfield, MN 55057, USA
- ⁶²Astronomical Observatory Warsaw University, 00-478 Warsaw, Poland
- ⁶³VU University Amsterdam, 1081 HV Amsterdam, The Netherlands
- ⁶⁴University of Maryland, College Park, MD 20742, USA
- ⁶⁵Laboratoire des Matériaux Avancés (LMA), CNRS/IN2P3, F-69622 Villeurbanne, France
- ⁶⁶Université Claude Bernard Lyon 1, F-69622 Villeurbanne, France
- ⁶⁷Università di Napoli ‘Federico II’, Complesso Universitario di Monte S. Angelo, I-80126 Napoli, Italy
- ⁶⁸NASA/Goddard Space Flight Center, Greenbelt, MD 20771, USA
- ⁶⁹RESCEU, University of Tokyo, Tokyo, 113-0033, Japan.
- ⁷⁰University of Adelaide, Adelaide, South Australia 5005, Australia
- ⁷¹Tsinghua University, Beijing 100084, China
- ⁷²Texas Tech University, Lubbock, TX 79409, USA
- ⁷³The University of Mississippi, University, MS 38677, USA
- ⁷⁴The Pennsylvania State University, University Park, PA 16802, USA
- ⁷⁵National Tsing Hua University, Hsinchu City, 30013 Taiwan, Republic of China
- ⁷⁶Charles Sturt University, Wagga Wagga, New South Wales 2678, Australia
- ⁷⁷University of Chicago, Chicago, IL 60637, USA
- ⁷⁸Kenyon College, Gambier, OH 43022, USA
- ⁷⁹Korea Institute of Science and Technology Information, Daejeon 305-806, Korea
- ⁸⁰University of Cambridge, Cambridge CB2 1TN, United Kingdom
- ⁸¹Università di Roma ‘La Sapienza’, I-00185 Roma, Italy
- ⁸²University of Brussels, Brussels 1050, Belgium
- ⁸³Sonoma State University, Rohnert Park, CA 94928, USA
- ⁸⁴Montana State University, Bozeman, MT 59717, USA
- ⁸⁵Center for Interdisciplinary Exploration & Research in Astrophysics (CIERA), Northwestern University, Evanston, IL 60208, USA
- ⁸⁶Universitat de les Illes Balears, IAC3—IEEC, E-07122 Palma de Mallorca, Spain
- ⁸⁷The University of Texas Rio Grande Valley, Brownsville, TX 78520, USA
- ⁸⁸Bellevue College, Bellevue, WA 98007, USA
- ⁸⁹Institute for Plasma Research, Bhat, Gandhinagar 382428, India
- ⁹⁰The University of Sheffield, Sheffield S10 2TN, United Kingdom
- ⁹¹California State University, Los Angeles, 5154 State University Dr, Los Angeles, CA 90032, USA
- ⁹²Università di Trento, Dipartimento di Fisica, I-38123 Povo, Trento, Italy
- ⁹³INFN, Trento Institute for Fundamental Physics and Applications, I-38123 Povo, Trento, Italy
- ⁹⁴Cardiff University, Cardiff CF24 3AA, United Kingdom
- ⁹⁵Montclair State University, Montclair, NJ 07043, USA
- ⁹⁶National Astronomical Observatory of Japan, 2-21-1 Osawa, Mitaka, Tokyo 181-8588, Japan
- ⁹⁷Canadian Institute for Theoretical Astrophysics, University of Toronto, Toronto, Ontario M5S 3H8, Canada
- ⁹⁸MTA Eötvös University, “Lendület” Astrophysics Research Group, Budapest 1117, Hungary
- ⁹⁹School of Mathematics, University of Edinburgh, Edinburgh EH9 3FD, United Kingdom
- ¹⁰⁰University and Institute of Advanced Research, Gandhinagar, Gujarat 382007, India

- ¹⁰¹IISER-TVM, CET Campus, Trivandrum Kerala 695016, India
 - ¹⁰²University of Szeged, Dóm tér 9, Szeged 6720, Hungary
 - ¹⁰³Embry-Riddle Aeronautical University, Prescott, AZ 86301, USA
 - ¹⁰⁴Tata Institute of Fundamental Research, Mumbai 400005, India
 - ¹⁰⁵INAF, Osservatorio Astronomico di Capodimonte, I-80131, Napoli, Italy
 - ¹⁰⁶University of Michigan, Ann Arbor, MI 48109, USA
 - ¹⁰⁷Rochester Institute of Technology, Rochester, NY 14623, USA
 - ¹⁰⁸NCSA, University of Illinois at Urbana-Champaign, Urbana, IL 61801, USA
 - ¹⁰⁹University of Białystok, 15-424 Białystok, Poland
 - ¹¹⁰SUPA, University of Strathclyde, Glasgow G1 1XQ, United Kingdom
 - ¹¹¹University of Southampton, Southampton SO17 1BJ, United Kingdom
 - ¹¹²University of Washington Bothell, 18115 Campus Way NE, Bothell, WA 98011, USA
 - ¹¹³Institute of Applied Physics, Nizhny Novgorod, 603950, Russia
 - ¹¹⁴Seoul National University, Seoul 151-742, Korea
 - ¹¹⁵Inje University Gimhae, 621-749 South Gyeongsang, Korea
 - ¹¹⁶National Institute for Mathematical Sciences, Daejeon 305-390, Korea
 - ¹¹⁷Pusan National University, Busan 609-735, Korea
 - ¹¹⁸NCBJ, 05-400 Świerk-Otwock, Poland
 - ¹¹⁹Institute of Mathematics, Polish Academy of Sciences, 00656 Warsaw, Poland
 - ¹²⁰Monash University, Victoria 3800, Australia
 - ¹²¹Hanyang University, Seoul 133-791, Korea
 - ¹²²The Chinese University of Hong Kong, Shatin, NT, Hong Kong
 - ¹²³University of Alabama in Huntsville, Huntsville, AL 35899, USA
 - ¹²⁴ESPCI, CNRS, F-75005 Paris, France
 - ¹²⁵University of Minnesota, Minneapolis, MN 55455, USA
 - ¹²⁶Università di Camerino, Dipartimento di Fisica, I-62032 Camerino, Italy
 - ¹²⁷Southern University and A&M College, Baton Rouge, LA 70813, USA
 - ¹²⁸The University of Melbourne, Parkville, Victoria 3010, Australia
 - ¹²⁹College of William and Mary, Williamsburg, VA 23187, USA
 - ¹³⁰Instituto de Física Teórica, University Estadual Paulista/ICTP South American Institute for Fundamental Research, São Paulo SP 01140-070, Brazil
 - ¹³¹Whitman College, 345 Boyer Avenue, Walla Walla, WA 99362 USA
 - ¹³²Université de Lyon, F-69361 Lyon, France
 - ¹³³Hobart and William Smith Colleges, Geneva, NY 14456, USA
 - ¹³⁴Janusz Gil Institute of Astronomy, University of Zielona Góra, 65-265 Zielona Góra, Poland
 - ¹³⁵King's College London, University of London, London WC2R 2LS, United Kingdom
 - ¹³⁶IISER-Kolkata, Mohanpur, West Bengal 741252, India
 - ¹³⁷Indian Institute of Technology, Gandhinagar Ahmedabad Gujarat 382424, India
 - ¹³⁸Andrews University, Berrien Springs, MI 49104, USA
 - ¹³⁹Università di Siena, I-53100 Siena, Italy
 - ¹⁴⁰Trinity University, San Antonio, TX 78212, USA
 - ¹⁴¹University of Washington, Seattle, WA 98195, USA
 - ¹⁴²Abilene Christian University, Abilene, TX 79699, USA
 - ¹⁴³Cornell Center for Astrophysics and Planetary Science, Cornell University, Ithaca, NY 14853, USA
-